Geochemistry, Geophysics, Geosystems®

AGU ADVANCING EARTH AND SPACE SCIENCE

RESEARCH ARTICLE
10.1029/2022GC010690

Key Points:

- We analyze three different types of geophysical observations beneath the Central Appalachian Mountains
- The upper mantle exhibits anomalies in its seismic velocity, seismic attenuation, and electrical conductivity structure
- Forward modeling shows that 1%–2% partial melt in the upper mantle can explain the geophysical observations

Correspondence to:
M. D. Long,
maureen.long@yale.edu

Citation:
Mittal, V., Long, M. D., Evans, R. L., Byrnes, J. S., & Bezada, M. (2023). Joint analysis of seismic and electrical observables beneath the Central Appalachians requires partial melt in the upper mantle. *Geochemistry, Geophysics, Geosystems*, *24*, e2022GC010690. https://doi.org/10.1029/2022GC010690

Received 7 SEP 2022
Accepted 12 JAN 2023

Joint Analysis of Seismic and Electrical Observables Beneath the Central Appalachians Requires Partial Melt in the Upper Mantle

Ved Mittal[1], Maureen D. Long[1], Rob L. Evans[2], Joseph S. Byrnes[3], and Maximiliano Bezada[4]

[1]Department of Earth and Planetary Sciences, Yale University, New Haven, CT, USA, [2]Department of Geology and Geophysics, Woods Hole Oceanographic Institution, Woods Hole, MA, USA, [3]School of Earth and Sustainability, Northern Arizona University, Flagstaff, AZ, USA, [4]Department of Earth and Environmental Sciences, University of Minnesota, Minneapolis, MN, USA

Abstract The Central Appalachian Anomaly (CAA) is a region of the upper mantle beneath eastern North America that exhibits pronounced anomalies in its seismic velocity, seismic attenuation, and electrical conductivity structure. The CAA clearly expresses itself in low velocity, high attenuation, and high conductivity values; however, the present-day composition and state of the asthenospheric upper mantle in the anomalous region remains imperfectly known. The collection of data from densely spaced, co-located seismic and magnetotelluric arrays during the Mid-Atlantic Geophysical Integrative Collaboration (MAGIC) experiment affords the opportunity to probe the structure and properties of the upper mantle in the CAA region in detail using multiple types of geophysical observations. Here, we present new observations of *P* and *S* wave travel times from teleseismic earthquakes measured at MAGIC stations, including a determination of how travel times deviate from the predictions of a standard 1-D reference model. These observations constrain the ratio of the *P* to *S* wave travel time perturbations associated with the CAA, which in turn allows us to estimate the ratio of *P* and *S* wave velocity anomalies. We combine these observations with previously published estimates of seismic attenuation and electrical conductivity in the upper mantle beneath the MAGIC array, and carry out forward modeling to determine reasonable ranges of temperature, partial melt fraction, water content, and composition for the CAA. Our results suggest that 1%–2% partial melt is required to simultaneously explain the velocity, attenuation, and electrical conductivity observations beneath the MAGIC array.

1. Introduction

Understanding the composition and state of the upper mantle remains a fundamental outstanding problem in the study of the Earth's interior. Variables such as the mineralogy/composition, temperature, water content, and (if present) partial melt fraction and configuration play key roles in controlling upper mantle rheology and dynamics. It is particularly important to understand these variables in regions of the upper mantle that are anomalous or unusual, as such regions are often associated with processes (e.g., intraplate volcanism) that are not predicted by simple plate tectonic theory. However, reliably estimating quantities such as the temperature, water content, and melt fraction in the upper mantle remains an enormous challenge for observational geophysics. While geophysical observables such as seismic velocity, seismic attenuation, and electrical conductivity are sensitive to these quantities, their interpretation is typically non-unique, and the uncertainties in translating laboratory experiments to the real Earth are large. A promising strategy for constraining these variables more tightly in regions of interest is to combine co-located observations of seismic velocity, seismic attenuation, and/or electrical conductivity (e.g., Artemieva et al., 2004; Iwamori et al., 2021; Moorkamp et al., 2007), taking advantage of the fact that these observables have different sensitivities to factors such as temperature, partial melt, water content, and composition (e.g., Cammarano et al., 2003; Dai & Karato, 2014; Faul et al., 2004; Jacobsen et al., 2008; Takei, 2002).

The Central Appalachian Anomaly (CAA; Figure 1), a pronounced upper mantle geophysical anomaly beneath the eastern seaboard of the United States, is a particularly intriguing target region for such a study. The eastern margin of North America is a passive continental margin, with the last major tectonic episode, the breakup of the Pangea supercontinent, occurring 200 Myr ago. Previous work, summarized by Long et al. (2021), has documented a number of unusual aspects of the CAA that are not typical in a passive margin setting. These include low upper mantle velocities in seismic tomography models (e.g., Porter et al., 2015; Schmandt & Lin, 2014; Wagner et al., 2018; Figure 1), high upper mantle seismic attenuation (Byrnes et al., 2019), high upper mantle electrical

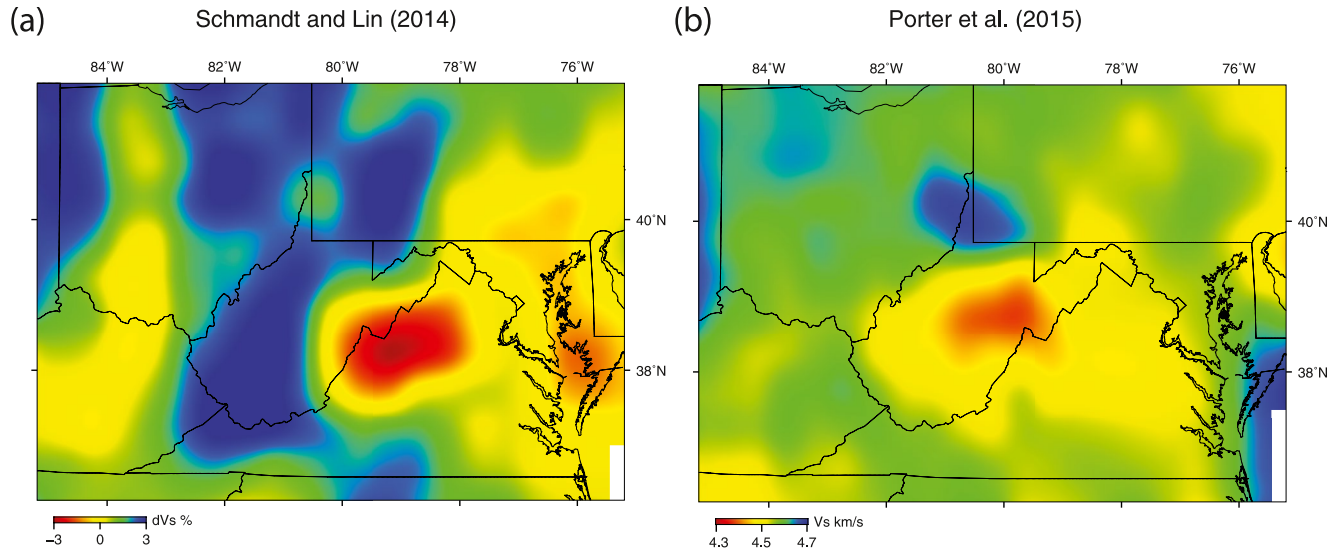

Figure 1. Horizontal slices through the *S* wave tomographic models of (a) Schmandt and Lin (2014) and (b) Porter et al. (2015) at a depth of 90 km. Colors represent relative shear wave velocity variations in panel (a) and absolute V_s values in panel (b), as denoted by the colorbars. Thin black lines show the boundaries of U.S. states. The prominent low velocity anomaly near the center of the image is the Central Appalachian Anomaly.

conductivity (Evans et al., 2019), unusually thin lithosphere (Byrnes et al., 2019; Evans et al., 2019), and an abrupt lateral transition in upper mantle anisotropy as reflected in *SKS* splitting (Aragon et al., 2017). Beyond the geophysical anomaly, unusual aspects of the CAA region include the occurrence of anomalously young volcanism that post-dates the breakup of Pangea, with volcanic and magmatic rocks from the late Jurassic and Eocene occurring in western Virginia and eastern West Virginia (e.g., Mazza et al., 2014, 2017), and unusually high present-day erosion rates (Long et al., 2021). Both the unusually young magmatic products and the enhanced erosion rates are co-located with the geophysical anomaly in the upper mantle.

The anomalously low seismic velocities, high seismic attenuation, and high electrical conductivity that are characteristic of the CAA may be individually explained by a range of possible upper mantle material properties, potentially including elevated temperatures, the presence of partial melt, high water content, and compositional variability. While previous work has suggested that partial melt is likely needed to explain the attenuation and electrical conductivity observations (Byrnes et al., 2019; Evans et al., 2019), these studies have acknowledged that the interpretation of the geophysical observables is non-unique, and that alternative explanations may be possible. The goal of this study is to combine three types of geophysical observations (*P* and *S* body wave travel time residuals, seismic attenuation as inferred from *P* waveforms, and an electrical conductivity model derived from magnetotelluric [MT] data) and incorporate these constraints into a set of quantitative models that constrain the range of plausible upper mantle temperatures, compositions, water contents, and partial melt fractions in the asthenospheric upper mantle of the CAA.

To do this, we use data from the Mid-Atlantic Geophysical Integrative Collaboration (MAGIC) geophysical array (Long et al., 2020). The MAGIC array, part of the EarthScope USArray Flexible Array, consisted of co-located linear deployments of 28 broadband seismic stations and 25 MT stations. The seismometers collected data between October 2013 and October 2016, while the MT instruments collected data between October 2015 and May 2016. The MAGIC stations (Figure 2), deployed in a NW-SE trending line across the U.S. states of Virginia, West Virginia, and Ohio, provide dense sampling from near the coast into the North American continental interior and cross the region of the CAA. Data from MAGIC have already been used to probe seismic attenuation (Byrnes et al., 2019) and electrical conductivity (Evans et al., 2019) across the profile. Specifically, Byrnes et al. (2019) identified a region of elevated attenuation directly underneath the Appalachians Mountains. They inferred a range of possible values of Q_P obtained from differential attenuation Δt_P^* and found that Q_P in the CAA upper mantle likely ranges between 50 and 63. Evans et al. (2019) obtained both 2-D and 3-D electrical conductivity models and identified thin lithosphere (~80 km) and a highly conducting region in the depth range between ~80 and 200 km beneath the Appalachian Mountains. Upper mantle electrical conductivity values associated with the CAA were inferred to be around 0.1 S/m (Evans et al., 2019).

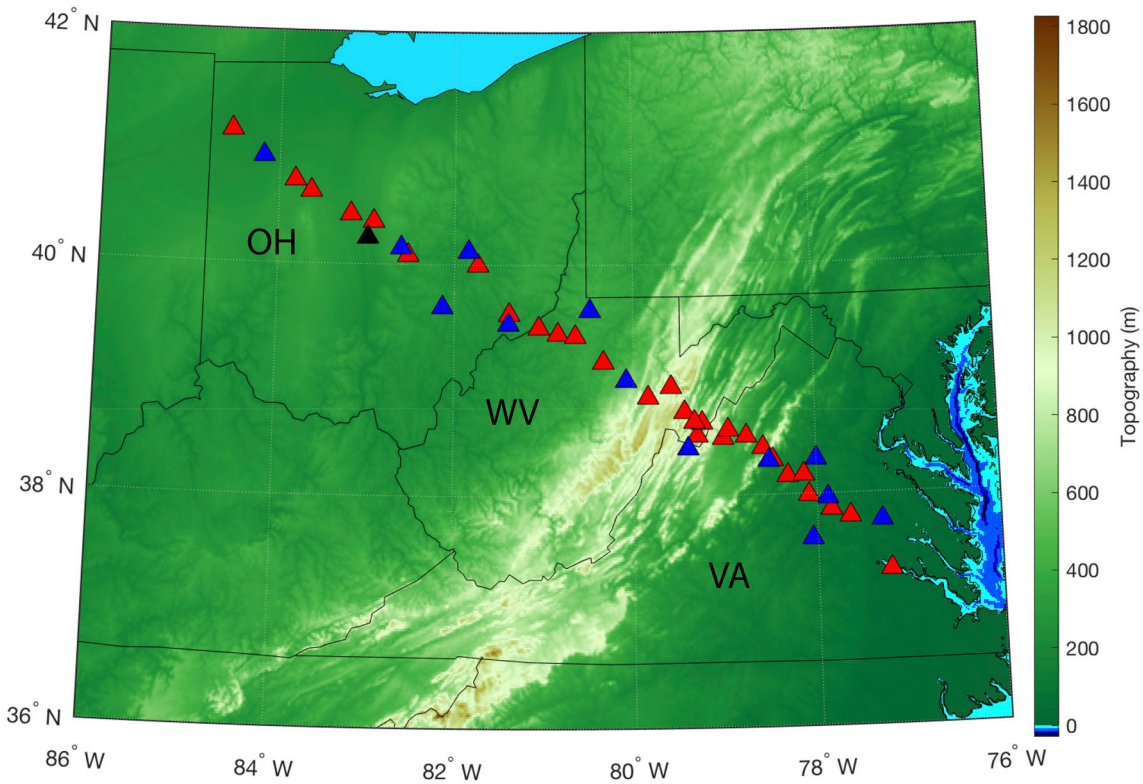

Figure 2. Map of seismic stations (triangles) used in this study. Background colors indicate topography, as shown by the colorbar at right. Thin black lines show the outlines of U.S. states, with labels indicating the states of Virginia (VA), West Virginia (WV), and Ohio (OH). We used a total of 42 broadband stations, including stations from the Mid-Atlantic Geophysical Integrative Collaboration experiment (red), the USArray Transportable Array (blue), and the U.S. National Seismic Network (black).

Constraints on the magnitude of the CAA upper mantle velocity anomaly have previously been obtained from seismic tomography (e.g., Babikoff & Dalton, 2019; Biryol et al., 2016; Boyce et al., 2019; Golos et al., 2018; Porter et al., 2015; Savage et al., 2017; Schmandt & Lin, 2014; Shen & Ritzwoller, 2016; Wagner et al., 2018). While the precise amplitude of the CAA anomaly varies among different studies, tomographic models have identified shear velocities as low as 4.3–4.4 km/s in the uppermost mantle from surface wave models (e.g., Wagner et al., 2018), and body wave tomography indicates relative velocity values that are ∼4%–5% slower than average for *S* waves and ∼2.5%–3% slower for *P* waves at a depth of 200 km (e.g., Schmandt & Lin, 2014). It can be challenging, however, to accurately infer the amplitude of velocity anomalies from seismic tomography models. Tomographic inversions employ strategies such as damping and smoothing, which means that the amplitudes of velocity anomalies are typically underestimated. Furthermore, different ray coverage for *P* and *S* waves means that a direct comparison between the amplitude of V_p and V_s anomalies in tomographic models is not straightforward. This is a significant limitation, as the relative size of *P* and *S* wave velocity perturbations can contain important information about the physical properties of the anomalous material. Estimates of the relative amplitudes of *P* and *S* wave velocity anomalies can, however, be obtained from measurements of travel time residuals associated with *P* and *S* wave arrivals across a seismic array (e.g., Menke et al., 2016). Such an approach is particularly useful in cases in which the geometry of the anomaly has been generally well constrained via seismic tomography. Estimates of body wave travel time residuals (i.e., deviations from measured arrival times and those predicted by a simple 1-D Earth model) can provide more direct estimates of the relative size of *P* and *S* wave anomalies than comparisons of *P* and *S* wave tomographic images. This type of approach is very well suited for the CAA study area, as the location and dimensions of the velocity anomaly have already been well characterized by tomographic imaging (Long et al., 2021, and references therein).

The goals of this work are twofold. First, we obtain new constraints on the relative *P* and *S* wave velocity perturbations in the upper mantle associated with the CAA by measuring *P* and *S* wave travel times from teleseismic earthquakes. Our approach follows that of Menke et al. (2016; see also Carrero Mustelier & Menke, 2021; Krauss

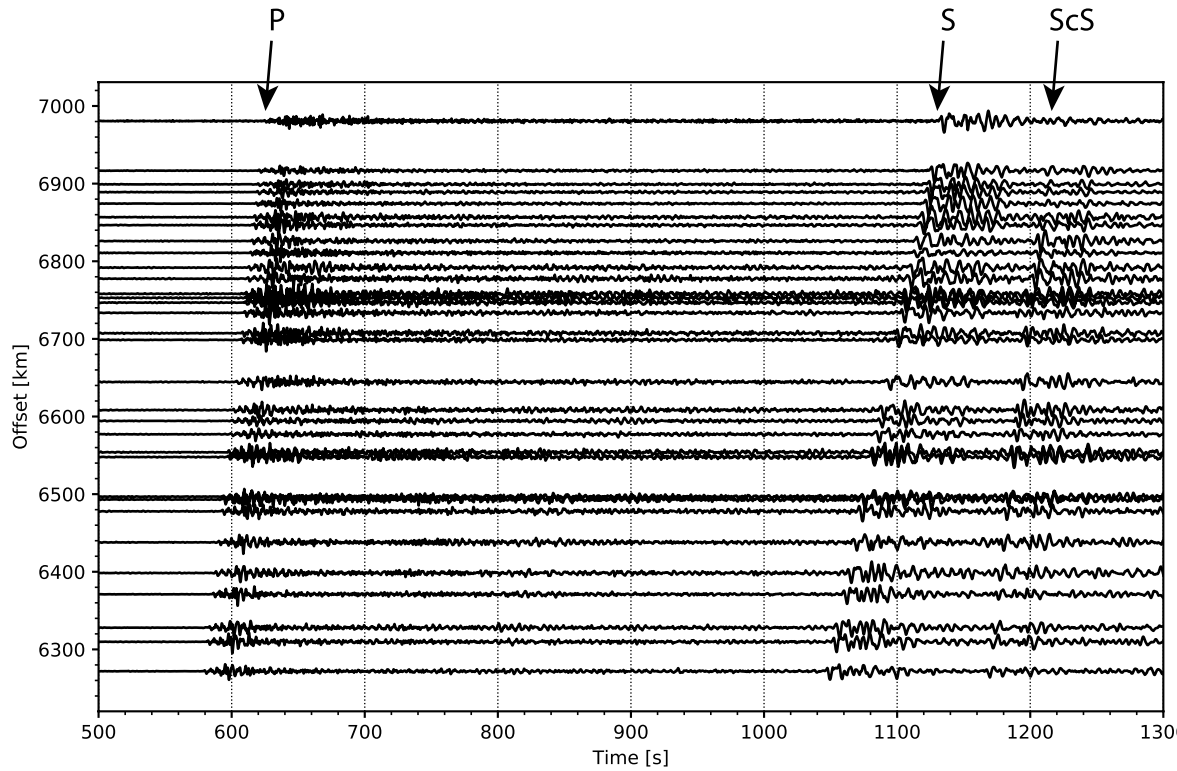

Figure 3. Record section (seismograms plotted as a function of increasing distance from the source) showing body wave arrivals on the horizontal component (BHE channel) for a 6.9 M_W earthquake beneath the Aleutian Islands (52.28°, −169.54°) that occurred on 27 July 2015. The *x* axis indicates time since the event origin time. The first *P* wave arrives at approximately 580 s at the closest station, followed by the first *S* wave at approximately 1,045 s. The *ScS* phase follows shortly after the S wave arrival at about 1,165 s.

& Menke, 2020), who measured differential *P* and *S* wave travel times associated with the Northern Appalachian Anomaly (NAA), another prominent geophysical anomaly beneath eastern North America, this one centered beneath New England (e.g., Levin et al., 1995, 2018; Menke et al., 2016, 2018). Menke et al. (2016) calculated observed arrival time deviations by comparing measured teleseismic earthquake travel times against predictions from a 1-D Earth model using a cross-correlation approach. We apply this measurement strategy to data from the densely spaced MAGIC array in this study, allowing us to measure a large number of body wave arrival times and estimate the ratio of *P* and *S* wave velocity anomalies. Second, we combine our new estimates of *P* and *S* wave velocity anomaly ratios with previously published estimates of upper mantle seismic attenuation (Byrnes et al., 2019) and electrical conductivity (Evans et al., 2019) to carry out quantitative modeling of the asthenospheric upper mantle in the CAA region. Specifically, we consider what ranges of material properties (temperature, partial melt fraction, water content, and composition) are capable of simultaneously explaining the three different types of observations.

2. Body Wave Travel Time Residual Measurements: Data and Methods

We used data from the MAGIC experiment (28 stations), the USArray Transportable Array (13 stations), and the US National Seismic Network (1 station), for a total of 42 seismic stations (Figure 2). We considered earthquakes occurring between October 2014 and October 2016, the period during which most of the MAGIC stations were recording. We selected events with moment magnitude (M_W) of 5.7 or greater at epicentral distances between 40° and 80° and measured *P* and *S* wave arrivals for each event at each available station. All seismic signals were bandpass filtered between 0.1 and 1 Hz before analysis. An example of a record section showing body wave arrivals for an event used in this study showing clear *P* and *S* arrivals is shown in Figure 3.

Following the method of Menke et al. (2016), we measured deviations of the recorded *P* and *S* wave arrival times from the predicted arrival times for a standard 1-D Earth model (AK135; Kennett et al., 1995). Travel times will be affected by a number of aspects of crustal structure (in addition to the upper mantle structure that is the focus

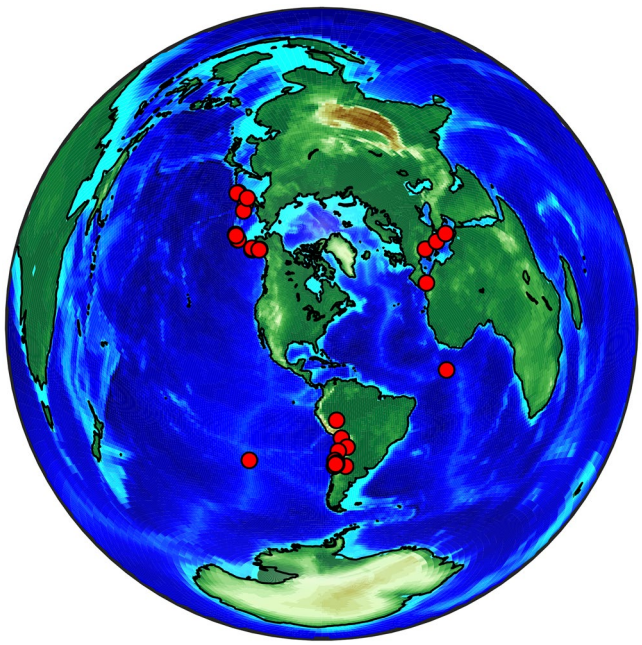

Figure 4. Map of events (red circles) used in this study. We used 35 high-quality events with moment magnitude $M_W \geq 5.7$ located at epicentral distances between 40° and 80° from the center of the Mid-Atlantic Geophysical Integrative Collaboration array.

of this study), potentially including crustal thickness variations, topography, and sedimentary basin structure. Of these, crustal thickness variations will have the largest effect; in contrast, the effects of topography and sedimentary basins are expected to be much smaller for our study region. We therefore corrected the predicted body wave arrival times to account for variations in crustal thickness. To do this, we used crustal thicknesses estimates obtained via *P*-to-*S* receiver function analysis at stations in our study region (Long et al., 2019). We compared the estimated crustal thickness beneath each station to the 35 km global crustal thickness average used in the AK135 model (Kennett et al., 1995). We predicted deviations in *P* and *S* wave travel times due to deviations from the 1-D model crustal thickness using nominal *P* and *S* wave velocities for the mantle ($V_P = 8.04\,\mathrm{km/s}$; $V_S = 4.48\,\mathrm{km/s}$) and crust ($V_P = 6.50\,\mathrm{km/s}$; $V_S = 3.85\,\mathrm{km/s}$) and used these to correct the predicted *P* and *S* wave arrival times, assuming vertical wave incidence. While the assumption of vertical incidence is a simplification, the errors introduced by this assumption are expected to be small compared to the uncertainties introduced by our imperfect knowledge of crustal thickness and velocity structure.

We designated the station with the first *P* and *S* wave arrival for each event as the "primary" station for that event. We then measured the difference in (both predicted and measured) arrival times for each station with respect to that of the "primary" station. The difference in measured arrival time between each station and the "primary" station was estimated using cross-correlation. The vertical component (BHZ channel) was used for the cross-correlation of *P* waves, while for *S* waves, we chose one of the horizontal components (BHE or BHN channel) for each event based on the prominence and clarity of the *S* wave arrival on each channel for that event. We obtained differential travel times estimates by comparing the differences in the predicted arrival times and recorded arrival times for each pair of stations.

We calculated differential travel times for *P* and *S* waves for pairs of stations for 35 well-recorded events (Figure 4). For each event, we subtracted the average *P* and *S* differential travel time to offset the average to zero (Krauss & Menke, 2020). The full set of zero-average *P* and *S* wave travel time residuals were used to produce a scatterplot, following Menke et al. (2016). We used Deming regression (Deming, 1943) to calculate the best-fit line through all measured differential travel times. Deming regression, also known as orthogonal regression, minimizes the sum of the squared perpendicular distances between the two *P* and *S* differential travel time data sets, therefore accounting for errors in both sets of measurements.

3. Body Wave Travel Time Residual Measurements: Results and Discussion

3.1. Estimates of *P* and *S* Travel Time and Velocity Anomaly Ratios

We produced maps of travel time residuals (with respect to the AK135 reference model) across the MAGIC study area for each event in our study. Examples for three different events from different backazimuths are shown in Figure 5. As discussed by, for example, Carrero Mustelier and Menke (2021), maps of travel time residuals for individual events arriving from different directions can shed light on the geographic location and depth extent of the anomaly; indeed, this notion underpins the method of body wave tomography. We find that events originating to the south of the array, such as the example event from northern Chile shown in Figures 5a and 5b, typically have the largest travel time residuals. In comparison, events originating to the east of the array, such as the example event from the Mid-Atlantic Ridge shown in Figures 5c and 5d, typically show travel time residuals that are smaller in magnitude and only exhibit significantly delayed *P* and *S* wave arrivals at stations located in the Appalachian Mountains. Body wave arrivals from events to the north of the array, such as the example event from the Kamchatka Peninsula shown in Figures 5e and 5f, also show delayed arrivals at stations located within the mountain range; delayed arrivals are also observed at stations in the easternmost portion of the array. Taken together, our observations of travel time residuals for all events are consistent with a low-velocity anomaly that is likely centered directly beneath or slightly east of the Appalachian Mountains and may extend significantly to the south of the MAGIC line, such that waves arriving from

10.1029/2022GC010690

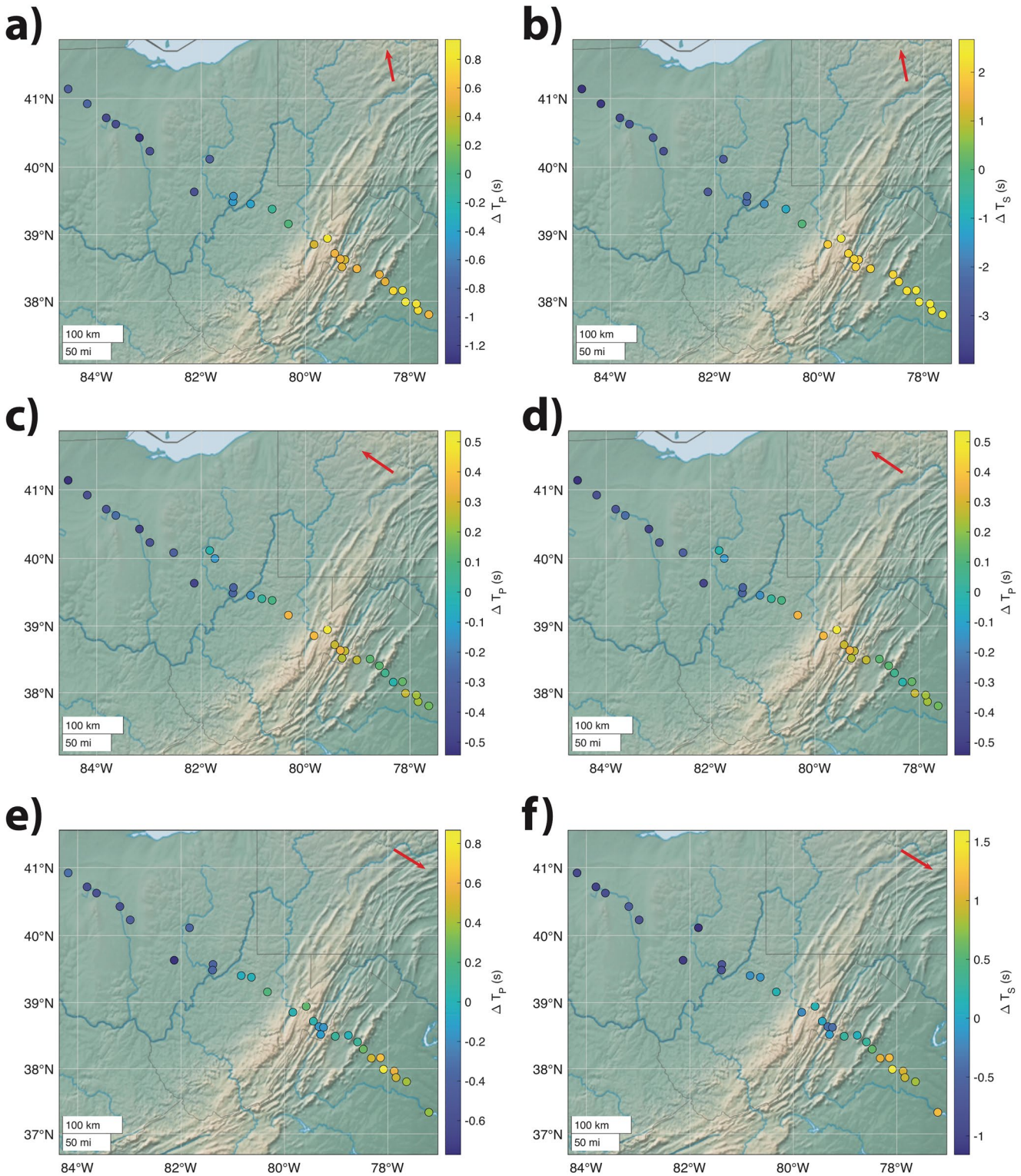

Figure 5.

the south accumulate more significant time delays than those arriving from the east or north. As expected, this is consistent with inferences from tomographic imaging of the CAA (see examples in Figure 1 and the discussion in Long et al. (2021)). It is possible that events arriving from the south and measured across the MAGIC line may also sample some portions of the so-called South Coastal Anomaly described by Carrero Mustelier

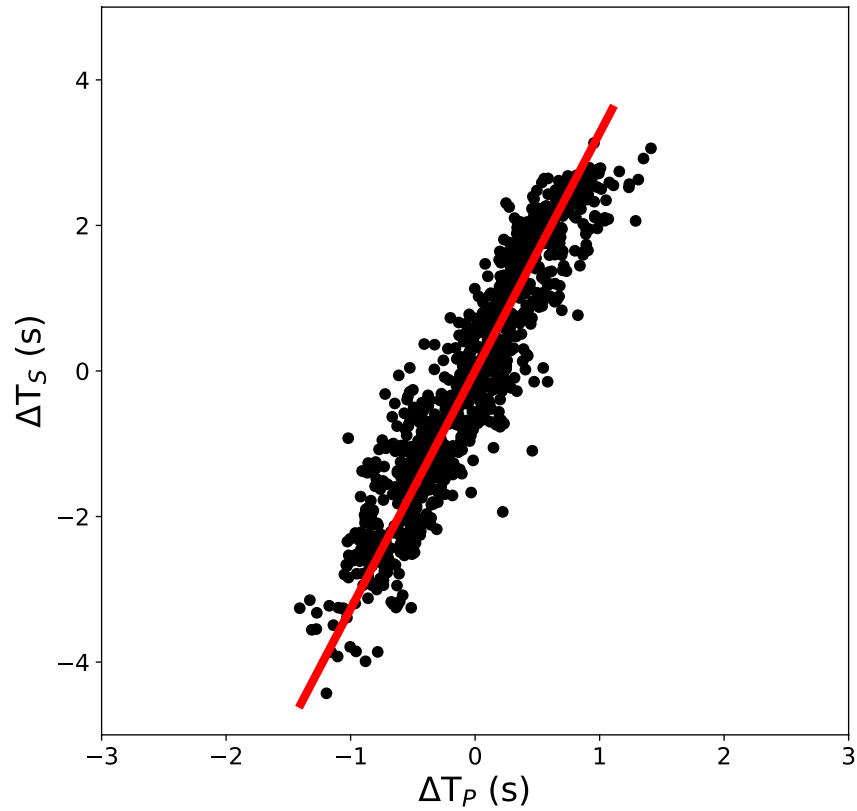

Figure 6. Scatterplot of P (x axis) and S (y axis) travel time residual measurements for all 35 earthquakes examined in this study. Red line indicates the best linear fit to the data, with a slope ($\Delta T_S/\Delta T_P$) of 3.269 ± 0.006.

and Menke (2021), a weaker and more diffuse zone of slow upper mantle velocities that lies to the south of the CAA itself.

Following Menke et al. (2016), we constructed a scatterplot (Figure 6) that compares travel time residuals for P (ΔT_P, x axis) and S (ΔT_S, y axis) wave arrivals for the entire data set. Because the only major upper mantle velocity anomaly beneath the region is the CAA (e.g., Porter et al., 2015; Schmandt & Lin, 2014), the bulk of the variability in the travel time residuals should be due to the presence of the CAA, and the slope of the line in Figure 6 mainly reflects the character of the CAA upper mantle. Furthermore, including both the slow CAA region as well as the more "standard" continental lithosphere beneath other parts of the MAGIC line in our calculation allows us to understand the properties of the slow region as compared to the non-perturbed region. The best-fitting line to these data, obtained via Deming regression after removing the mean from the data so that the line passes through the origin, yields an estimate of the ratio of the delay time residuals ($\Delta T_S/\Delta T_P$) of 3.269. From this, we estimate the ratio of the S to P wave velocity anomalies, again following Menke et al. (2016). A velocity perturbation Δv associated with a wave with a background velocity v_o traveling along a path of length H will produce a delay time ΔT, such that:

$$\Delta v = \frac{-\Delta T {v_o}^2}{H}. \quad (1)$$

Using the expression for Δv, the ratio of the S to P velocity anomalies is:

Figure 5. Single-event delay time residual maps for three different earthquakes. (a) P wave delay time residuals measured for a 6.2 M_W earthquake in northern Chile (−24.83°, −70.60°) that occurred on 27 November 2015. Circles show station locations, with the color indicating ΔT_P in s, according to the colorbar. Red arrow shows the propagation direction (azimuth) of the arriving waves. (b) S wave delay time residuals for the same earthquake as in panel (a), with colors indicating ΔT_S. (c) P wave delay time residuals measured for a 7.1 M_W earthquake along the Mid-Atlantic Ridge (−0.05°, −17.83°) that occurred on 29 August 2016. Plotting conventions are as in panel (a); however, note the difference in the color scale. (d) S wave delay time residuals for the same earthquake as in panel (c). Plotting conventions are as in panel (b); however, note the difference in the color scale. (e) P wave delay time residuals measured for a 7.2 M_W earthquake beneath the Kamchatka Peninsula (54.01°, 158.51°) that occurred on 30 January 2016. Plotting conventions are as in panel (a); however, note the difference in the color scale. (f) S wave delay time residuals for the same event as in panel (e). Plotting conventions are as in panel (b); however, note the difference in the color scale.

$$\frac{\Delta v_S}{\Delta v_P} = \left(\frac{\Delta T_S}{\Delta T_P}\right)\left(\frac{v_{oS}}{v_{oP}}\right)^2 \quad (2)$$

For this calculation, we assume a nominal depth of the velocity anomaly to be 200 km, based on the tomography model of Schmandt and Lin (2014). Using the AK135 model velocities at a depth of 210 km ($v_P = 8.300$ km/s; $v_S = 4.518$ km/s), and the $\Delta T_S/\Delta T_P$ value of 3.269 estimated from Figure 6, we estimate the ratio of the *S* and *P* wave velocity anomalies ($\Delta v_S/\Delta v_P$) in the upper mantle of the CAA as 0.969. This ratio is not dissimilar to that determined at similar upper mantle depths by Menke et al. (2016) for the NAA (1.18 ± 0.08) and to that estimated by Krauss and Menke (2020) for the Northern Gulf Anomaly, another low velocity anomaly beneath eastern North America (1.03 ± 0.20).

In addition to calculating $\Delta v_S/\Delta v_P$ from the scatterplot in Figure 6, we can also use the maximum values of observed differential travel times (without the mean removed) to obtain a rough estimate of the amplitude of the *P* and *S* wave velocity anomalies. This allows us to estimate the likely maximum velocity reduction associated with the CAA velocity anomaly, which in turn will help us to constrain the plausible range of temperatures, compositions, and melt fractions for the region (Section 4). The maximum observed differential travel times for delayed arrivals that have sampled the slow upper mantle velocity anomaly in our work are 2.07 s for *P* waves and 6.36 s for *S* waves. From these values, we can estimate the maximum velocity reduction, following the arguments in Menke et al. (2016) and making some assumptions about the depth range of the anomaly from previous tomographic imaging. Maximum velocity reductions for these differential travel times can be estimated by rearranging Equation 1 (Menke et al., 2016):

$$\frac{\Delta v}{v_o} = \frac{-\Delta T v_o}{H}, \quad (3)$$

where ΔT is the largest absolute delay time measured for *P* and *S* waves respectively. Menke et al. (2016) used this relationship to argue that their maximum *S* wave delay time (~6.8 s) could be explained by a ~10% reduction in *S* wave velocities associated with the NAA. For the CAA, we estimate that if the CAA velocity perturbation is distributed over a 200 km thick mantle column, the *P* and *S* wave velocity reductions would be about 8.2% for *P* waves and 13.7% for *S* waves. If the velocity perturbation was distributed over a 300 km thick column of mantle, then the velocity perturbations would be smaller (~5.5% for P and 9.1% for S). This range of estimates (200–300 km) for the vertical extent of the CAA velocity anomaly is consistent with recent detailed tomographic imaging using MAGIC data (Lee, 2021), which suggests that the anomaly extends to ~200 km depth directly beneath the Central Appalachians Mountains and ~300 km depth just to the east.

3.2. Errors and Uncertainties

A large number of factors contribute to uncertainties on our estimates of $\Delta T_S/\Delta T_P$ and $\Delta v_S/\Delta v_P$ for the CAA upper mantle. These include the measurement uncertainties on the *P* and *S* wave cross-correlation arrival time estimates themselves, which may be as high as tenths of a second, as well as other factors such as so-called signal-generated noise (distortion in pulse shapes), uncertainties in crustal structure, and the presence of seismic anisotropy (discussed in Section 3.3). It is evident from Figure 6 that there is considerable scatter in the $\Delta T_S/\Delta T_P$ data set, reflecting these uncertainties; the level of scatter in our data is comparable to similar data sets (Carrero Mustelier & Menke, 2021; Krauss & Menke, 2020; Menke et al., 2016). We determined a simple estimate of the error on the slope of the line in Figure 6 via a bootstrap resampling approach; we calculated a 95% confidence interval using the standard deviation of the calculated slope values for 100 runs, in which each run randomly sampled 60% of the differential travel time data. This exercise yields an error estimate of ±0.006 (95% confidence interval); however, given that this does not take into account measurement uncertainties or other factors, this is a considerable underestimate of the actual error. Following Menke et al. (2016), and taking into account the measurement uncertainties and the assumptions made in the crustal corrections, we estimate that our uncertainties on our $\Delta T_S/\Delta T_P$ value of 3.269 are at least as large as those estimated by Menke et al. (2016), and perhaps somewhat larger, given the significant variability in crustal structure along the MAGIC line (Long et al., 2019). Following the arguments in Menke et al. (2016), we estimate that the 95% confidence region on our $\Delta T_S/\Delta T_P$ is at least ±0.3; an additional source of error that is introduced in our estimate of $\Delta v_S/\Delta v_P$ is our use, again following Menke et al. (2016), of a nominal depth of 200 km for

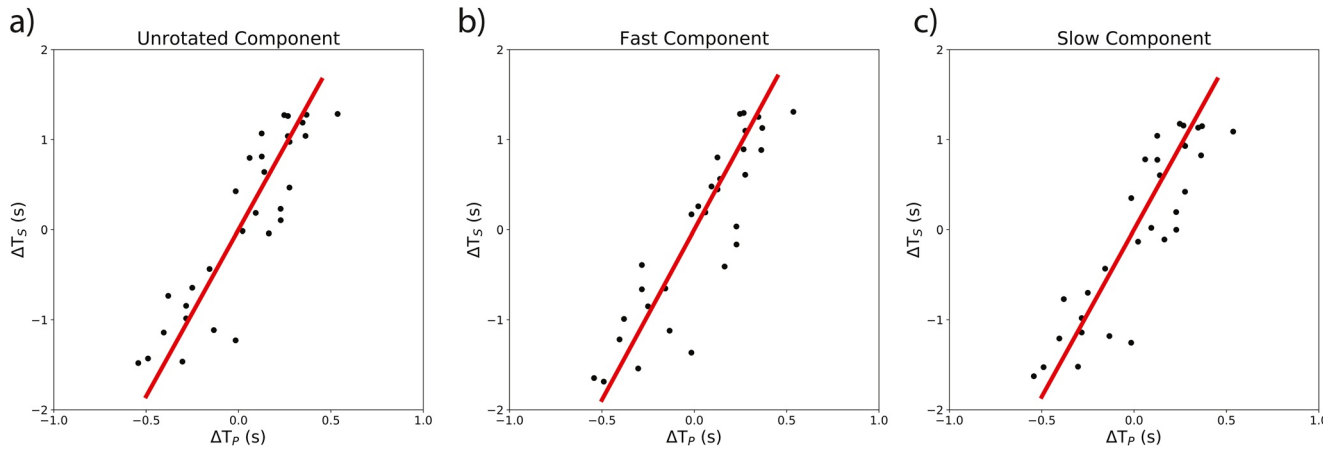

Figure 7. Investigation of the possible effects of upper mantle anisotropy on our $\Delta T_S/\Delta T_P$ estimates. Data from a 7.1 M_W earthquake along the Mid-Atlantic Ridge ($-0.05°$, $-17.83°$) that occurred on 29 August 2016 are used. (a) Scatterplot of P (x axis) and S (y axis) travel time residual measurements, with S wave arrival times measured from the unrotated horizontal component. Red line indicates the best linear fit to the data. Panel (b) same as panel (a), but using the horizontal component rotated to the average fast splitting direction across the Mid-Atlantic Geophysical Integrative Collaboration array. Panel (c) same as panel (a), but using the horizontal component rotated to the slow splitting direction. The estimated slopes for the three components are within 2.5% of each other.

the velocity anomaly rather than integrating over the upper mantle column that contains the anomaly (whose depth range is itself uncertain). We estimate that this propagates into an error of ± 0.15 on $\Delta v_S/\Delta v_P$ in our study.

3.3. Possible Effects of Seismic Anisotropy

Lattice-preferred orientation of anisotropic minerals in the upper mantle often causes seismic anisotropy (e.g., Karato et al., 2008), which may potentially affect any differential travel time measurements. Here, we investigate the possible effects of seismic anisotropy on our estimates of P and S velocity anomaly ratios beneath our study region. First, we consider the amplitude of potential body wave travel time anomalies due to the effect of upper mantle anisotropy. Levin et al. (1996) estimated that P wave travel time anomalies of approximately 0.2–0.3 s should correspond to S wave splitting delay times of about 1 s for lateral variations in upper mantle anisotropy. Long et al. (2016) and Aragon et al. (2017) documented *SKS* splitting delay times of roughly 1 s or less throughout the MAGIC study area; however, the documented P wave travel time anomalies in this study are roughly an order of magnitude larger than the corresponding P wave anomalies predicted for anisotropy by Levin et al. (1996). It is unlikely, therefore, that upper mantle anisotropy makes a major contribution to the travel time residuals we document in this study.

In order to further confirm this impression, we selected a few events and measured the S wave arrival times on both the fast and the slow horizontal components to verify that the estimated slope of the ΔT_S versus ΔT_P scatterplot does not depend on whether the fast or slow quasi-S waves were measured. For this exercise, we computed an average fast direction across the MAGIC array from the work of Aragon et al. (2017). Fortunately, the fast directions do not vary drastically across the array; dominantly NE-SW fast directions are observed in the western part of the study area, with a clockwise rotation to more nearly E-W fast directions in the east (Aragon et al., 2017). We then rotated the horizontal components to the average fast and slow directions and measured the S wave differential travel times for each component using cross-correlation. Scatterplots of differential travel times measured on each component for an example event (located along the Mid-Atlantic Ridge) are shown in Figure 7. This example demonstrates that the differences in the P and S wave travel time residual ratios among the fast, slow, and unrotated horizontal components are not significant; specifically, the estimated slopes for the three components are within 2.5% of each other, much smaller than the likely level of uncertainty introduced by other factors (Section 3.2). This is true for the entire subset of events we considered in this test, thereby providing further confirmation that seismic anisotropy does not strongly influence the travel time residual estimates in this study.

4. Modeling of Travel Time, Seismic Attenuation, and Electrical Conductivity Measurements

Our next step is to use the insights into P and S wave velocity anomaly ratios gleaned from travel time residual measurements to understand the physical state of the asthenospheric upper mantle in the CAA region. Our approach combines the interpretation of our velocity perturbation estimates with previous measurements of seismic attenuation (Byrnes et al., 2019) and electrical conductivity (Evans et al., 2019) across the MAGIC profile. For each of our three observables (seismic velocities, seismic attenuation, and electrical conductivity), we determine the range of temperatures, melt fractions, water contents, and compositions (specifically variations in Fe number) that would be needed to plausibly explain the observations. We then consider the suite of observations as a whole and investigate what effect (or combination of effects) is most likely to explain the anomalous structure of the CAA upper mantle.

4.1. *P* and *S* Wave Velocity and Travel Time Perturbations

We first explore the range of asthenospheric upper mantle conditions that can explain the travel time residual measurements for P and S waves discussed in Section 3. Our measurements reveal an estimated ratio of the velocity anomalies ($\Delta v_S/\Delta v_P$) at 210 km depth of 0.969 ± 0.15, with maximum estimated velocity reductions of ~9.1%–13.7% for S waves.

4.1.1. Effects of Temperature

Seismic wave velocity perturbations can be caused by temperature anomalies, and temperature is often invoked as the primary explanation for seismic velocity heterogeneity in the upper mantle. Cammarano et al. (2003) examined the combined effects of anharmonicity and anelasticity on seismic wave velocities from previously published mineral physics data to determine temperature derivatives for v_P and v_S as a function of depth. The model by Cammarano et al. (2003) estimates a value for $\partial \ln v_S/\partial \ln v_P$ of 1.73 at 200 km depth along a 1300°C adiabat, which translates to a $\Delta v_S/\Delta v_P$ value of 0.94. The similarity between the $\Delta v_S/\Delta v_P$ value of 0.969 ± 0.15 from this study and the one predicted by Cammarano et al. (2003) suggests that the velocity perturbations associated with the CAA can potentially be explained purely in terms of temperature. Velocity anomaly ratios of 1.18 ± 0.08 and 1.03 ± 0.20 that have previously been determined for other low velocity anomalies in the upper mantle beneath eastern North America (the NAA and the NGA, respectively) have also been interpreted as being due to thermal anomalies (Krauss & Menke, 2020; Menke et al., 2016), based on the model of Cammarano et al. (2003). We note that this model uses a range of possible anelasticity values for the upper mantle that are consistent with global seismic data (e.g., Romanowicz & Durek, 2000), with Q_s values that range from ~50 to 250 in the 100–300 km depth range.

Another model that can be used to determine whether our observed $\Delta v_S/\Delta v_P$ values are consistent with purely thermal perturbations is that of Karato (1993), who provides temperature derivatives for seismic velocities due to both anharmonic and anelastic effects. Equation 6 from Karato (1993) allows us to calculate temperature derivatives for seismic velocities that are specific to the attenuation profile of the CAA. The temperature derivatives for seismic velocities (Equations 6 and 7 from Karato (1993)) is represented as:

$$\frac{\partial \ln v}{\partial T} = \frac{\partial \ln v_o}{\partial T} - \left(\frac{\pi\alpha}{2}\right)\cot\left(\frac{\pi\alpha}{2}\right)\left(\frac{Q^{-1}(\omega,T)}{\pi}\right)\left(\frac{H^*}{RT^2}\right) \tag{4}$$

where v_o is the unrelaxed reference velocity, α is the frequency dependence of the quality factor Q, Q^{-1} is the attenuation, H^* is the activation enthalpy, and R is the gas constant. Use of this relationship requires explicit knowledge of the attenuation structure of the CAA. Estimates of seismic attenuation (discussed further in Section 4.2 below) from Byrnes et al. (2019) suggest Q_P values between 50 and 63 for the region, which correspond to Q_S values of 22 and 28 (assuming a Q_P/Q_S ratio of 2.25, following Karato and Spetzler (1990)). The temperature derivatives for seismic velocities due to anharmonic effects (first term of Equation 4), corresponding to infinite Q, are taken from Isaak (1992) and can be found in Table 1 of Karato (1993). Using the higher end of the range of allowed quality factors (Q_P of 63 and Q_S of 28) and assuming $T = 1600$ K, $\alpha = 0.2$, and $H^* = 500$ kJ/mol for olivine, we obtain:

$$\frac{\partial \ln v_P}{\partial T} = -1.77 \times 10^{-4}\ K^{-1} \tag{5}$$

$$\frac{\partial \ln v_S}{\partial T} = -3.34 \times 10^{-4}\ K^{-1} \quad (6)$$

$$\frac{\partial \ln v_S}{\partial \ln v_P} = 1.89 \quad (7)$$

This roughly corresponds to a $\Delta v_S/\Delta v_P$ value of 1.03 at 200 km depth. Since the temperature derivatives for seismic velocities using Karato (1993) are calculated using the attenuation measurements from Byrnes et al. (2019) for the region, the $\Delta v_S/\Delta v_P$ ratio differs slightly from the value predicted by the Cammarano et al. (2003) model, although it is still comparable to the 0.969 ± 0.15 value determined in this study. Therefore, both the Karato (1993) and Cammarano et al. (2003) models predict $\Delta v_S/\Delta v_P$ ratios for a purely thermal anomaly that are consistent with our observations.

We can also consider the magnitude of the temperature anomaly that would be required to explain the estimated maximum velocity reductions from our travel time data (ranging from 5.5% to 8.2% for *P* waves and 9.1%–13.7% for *S* waves). From Equations 5 and 6, we find that a temperature contrast of ∼410–460 K would be required to explain the maximum *P* and *S* wave velocity reductions we estimate (8.2% for *P* and 13.7% for *S*). At the lower end of the range (5.5% for *P* waves and 9.1% for *S* waves), a temperature contrast of ∼275 K would be needed to explain both types of data. As noted by Menke et al. (2016), the high temperature contrasts suggested by our travel time residual data seem somewhat extreme for a mature passive continental margin setting; furthermore, such contrasts would imply that the upper mantle temperature might be above the solidus, such that the presence of partial melt would also potentially have significant effect on the velocity reductions. Therefore, while we find that a thermal anomaly is consistent with the slope of our $\Delta T_S/\Delta T_P$ data (Figure 6), a particularly large temperature anomaly would be needed to explain the full range of ΔT_S and ΔT_P values that we document in the CAA region.

4.1.2. Effects of Partial Melt

The presence of partial melt in a system can greatly reduce seismic wave velocities. Moreover, the size and shape of the melt-filled pores are a significant factor in the magnitude of the velocity reduction. Takei (2002) studied the effect of partial melt on *P* and *S* wave velocities for different melt models that included a range of pore shapes and sizes. Takei (2002; see their Figure 2) demonstrated that for two particular models (the equilibrium geometry model and the oblate spheroid model), both the melt-solid dihedral angle and the aspect ratio significantly affect the elastic moduli of a material for a given melt fraction. For smaller values of the dihedral angle/aspect ratio, partial melt starts to form melt films, which completely wet grain boundaries and greatly reduce the material's elastic moduli. For higher values of the dihedral angle, partial melt tends to isolate itself within the grain triple junctions; in this geometry, melt does not affect the material's elastic moduli as much. A texturally equilibrated melt system, in which the melt network is configured such that the energy of the melt-solid interfaces is minimized (e.g., Rudge, 2018), should have a typical dihedral angle between 20° and 40° (corresponding to an aspect ratio of 0.1–0.15; Takei, 2002). For this range of dihedral angles, the $\partial \ln v_S/\partial \ln v_P$ ratio is 1–1.5. This translates to a $\Delta v_S/\Delta v_P$ value of 0.54–0.82 at 200 km depth, which is not in agreement with the $\Delta v_S/\Delta v_P$ value of 0.969 ± 0.15 we estimated from the travel time data.

However, Takei (2002) suggests that for regions with melt configurations involving structures such as dikes and veins, the melt system is not, in fact, in textural equilibrium. In such cases, the aspect ratio would be less than 10^{-2} and the *S*-wave velocities would be reduced far more than the *P*-wave velocities. It is possible that the Central Appalachians might be one of these regions. Such regions would have substantially higher $\partial \ln v_S/\partial \ln v_P$ ratios (between 1.7 and 2.3), which translates to a $\Delta v_S/\Delta v_P$ values between 0.93 and– 1.25 at 200 km depth, which would be in agreement with our measured ratio. Moreover, only a small melt fraction of about 1% would be required to explain the velocity reductions observed (Takei, 2002). We suggest, therefore, that the estimated $\Delta v_S/\Delta v_P$ values associated with the CAA could be explained by the presence of ∼1% partial melt if the melt system is far from textural equilibrium.

4.1.3. Effects of Water

Water incorporated into nominally anhydrous minerals, as hydrogen-related point defects, can also reduce seismic wave velocities, although the effect of water on the reduction of elastic moduli is generally small, as shown

by laboratory experiments performed on hydrous olivine by Jacobsen et al. (2008). The estimated effect of water on seismic velocities is shown in Equations 4 and 5 from Jacobsen et al. (2008):

$$v_P = 8.35(\pm 0.01) - 0.035(\pm 0.002)C_{H2O} \tag{8}$$

$$v_S = 4.81(\pm 0.02) - 0.025(\pm 0.003)C_{H2O} \tag{9}$$

where $v_{P(S)}$ is the P wave (S wave) seismic velocity measured in km/s and C_{H2O} is the water content measured in weight percent. The velocity perturbation ratio for water-rich olivine is calculated using Equations 8 and 9 above would be

$$\frac{\Delta v_S}{\Delta v_P} = 0.71. \tag{10}$$

The $\Delta v_S / \Delta v_P$ value of 0.969 ± 0.15 obtained from the travel time data in this study is significantly higher than the velocity perturbation ratio using Jacobsen et al. (2008), suggesting that a local anomaly in water content is not a good explanation for our observations.

We note, additionally, that Equations 8 and 9 show that a water content of roughly 15 wt.% or greater would be required to explain even the lower end of our estimated range for the maximum S wave velocity reduction for the CAA (9.1%–13.7% for S waves). Such a water content is unrealistic for the upper mantle (indeed, it far exceeds the water solubility limit for olivine), again suggesting that the presence of water in the upper mantle cannot explain our observations of the CAA.

4.1.4. Effects of Composition

Seismic wave velocities are sensitive to compositional changes in mantle minerals. When associated with a change in Fe number, the compositional effect on seismic velocities is largely due to the density contrast between Fe and Mg; effects of Fe number on the elastic moduli for the forsterite-fayalite system are thought to be generally small (e.g., Nestola et al., 2011). Speziale et al. (2005) analyzed the effect of compositional changes, and in particular changes in Fe number, on seismic velocities using elasticity data from single-crystal experiments on mantle minerals. Table 3 from Speziale et al. (2005) shows the relations between seismic velocities and mineral composition at different temperature and pressure conditions. From Table 3 of Speziale et al. (2005) for olivine at 4 GPa and high T (for the high T case, values were calculated along an adiabat with 1673 K foot temperature [i.e., the temperature at zero depth]):

$$\frac{\partial \ln v_P}{\partial X_{Fe}} = -0.25 \tag{11}$$

$$\frac{\partial \ln v_S}{\partial X_{Fe}} = -0.39 \tag{12}$$

$$\frac{\partial \ln v_S}{\partial \ln v_P} = 1.56 \tag{13}$$

The velocity perturbation ratio ($\Delta v_S / \Delta v_P$) calculated using Equation 13 (Speziale et al., 2005) yields a value of 0.85 at 200 km depth, which is inconsistent with the ratio determined from the travel time data of 0.969 ± 0.15 except at the low end of the range predicted by our error estimates. Therefore, compositional changes, as expressed by a change in Fe number, are not a likely explanation for our observations in the CAA region, although they cannot completely be ruled out.

4.2. Seismic Attenuation

Byrnes et al. (2019) used teleseismic P waves to determine the 1-D attenuation profile of the CAA across the MAGIC array. Byrnes et al. (2019) estimated the attenuation parameter Δt_P^*, which measures the differential attenuation of a P wave, and used these values to produce estimates of Q_P in the asthenospheric upper mantle. The preferred model from Byrnes et al. (2019), showing variations in Δt_P^* across the MAGIC array, is shown in Figure 8. Byrnes et al. estimated Q_P values between 50 and 63 beneath the Central Appalachians (associated with the CAA anomaly) and 103 to 125 to the east of the Appalachian mountain range. Using the nominal Q_P/Q_S

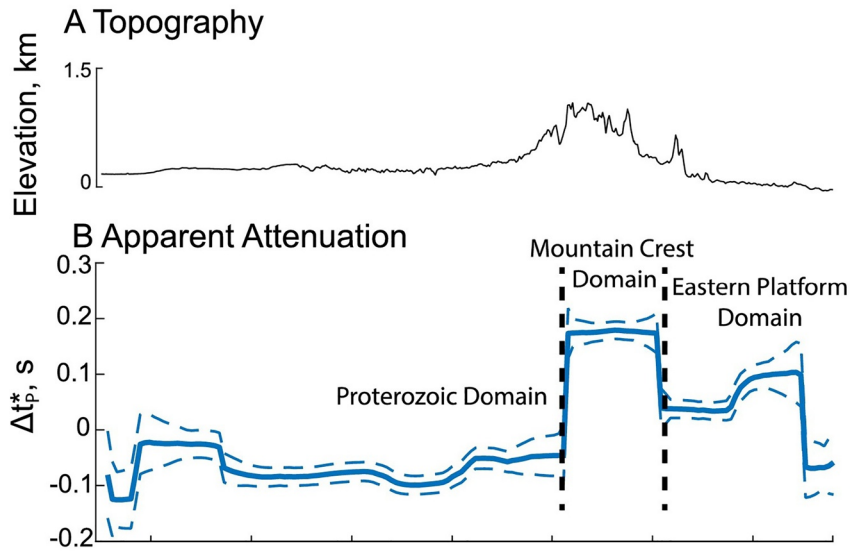

Figure 8. Attenuation measurements across the Mid-Atlantic Geophysical Integrative Collaboration array, adapted from Byrnes et al. (2019). (a) Topographic cross-section across the study region. (b) Model of best-fitting apparent *P* wave attenuation parameter (Δt_P^*; thick blue line) across the MAGIC array. The Mountain Crest Domain region (bounded by black dashed lines) corresponds to the anomalously high attenuation associated with the Central Appalachian Anomaly. Dashed blue lines show the uncertainty estimates on Δt_P^*.

ratio of 2.25 from Karato and Spetzler (1990), these values imply that Q_S ranges between 22 and 28 ($10^{-1.45}$ to $10^{-1.35}$ for ${Q_S}^{-1}$) for the CAA.

The results of Byrnes et al. (2019) are valid only so far as the apparent attenuation of the *P* phases reflects the intrinsic attenuation of the mantle. However, two mechanisms for extrinsic attenuation are well documented in the literature—scattering and focusing. In these scenarios, energy is not removed from the wavefield, but redistributed so as to cause the appearance of attenuation of a specific phase. Both mechanisms were rejected by Byrnes et al. (2019) as satisfactory explanations for the MAGIC observations on the basis of wavefield simulations. Scattering is caused by small-scale heterogeneities redistributing high frequency energy into the *P* wave coda (e.g., Richards & Menke, 1983). Significant artifacts in Δt_P^* for a ∼1 Hz *P* phase can be generated by small-scale, stochastic heterogeneities (∼±10%) for frequency domain approaches to Δt_P^*, but not for the time-domain method used with the MAGIC data set (Figure S6 in Byrnes et al. (2019), see also Bezada (2017) and Bezada et al. (2019) for discussion). Focusing artifacts in Δt_P^* occur when anomalies in velocity are of the right length-scale for finite-frequency effects to modulate the amplitude differently for different frequencies (Allen et al., 1999; Sigloch & Nolet, 2006). For 1 Hz *P* phases, plausible mantle structures generate small focusing artifacts that oscillate between positive and negative values over length-scales shorter than the anomaly in the CAA (Figure S8 in Byrnes et al., 2019). In fact, the velocity model of Schmandt and Lin (2014) predicts peak artifacts that are an order of magnitude smaller than the observational uncertainty.

Byrnes et al. (2019) argued that the high attenuation observed beneath the Central Appalachians cannot be solely explained by a plausible range of temperatures and grain sizes, implying that the CAA region exhibits near-solidus to super-solidus conditions and that melting or pre-melting processes contribute to the attenuation. Byrnes et al. (2019) suggested that the attenuation observations could either be explained by the presence of partial melt, or by a mechanism proposed by Yamauchi and Takei (2016) that predicts an enhancement in attenuation of seismic waves when temperatures approach the solidus. Here, we revisit and expand on the discussion in Byrnes et al. (2019), reproducing some of their calculations for completeness and also considering the potential role of additional factors (variability in water content and composition).

4.2.1. Effects of Temperature

High temperatures enhance anelasticity, as shown by Jackson and Faul (2010) in their experiments studying attenuation in melt-free olivine as a function of temperature and grain size. Following Byrnes et al. (2019), we use the Very Broadband Rheology Calculator (Havlin et al., 2021; Holtzman, 2016) to determine ${Q_S}^{-1}$ according to

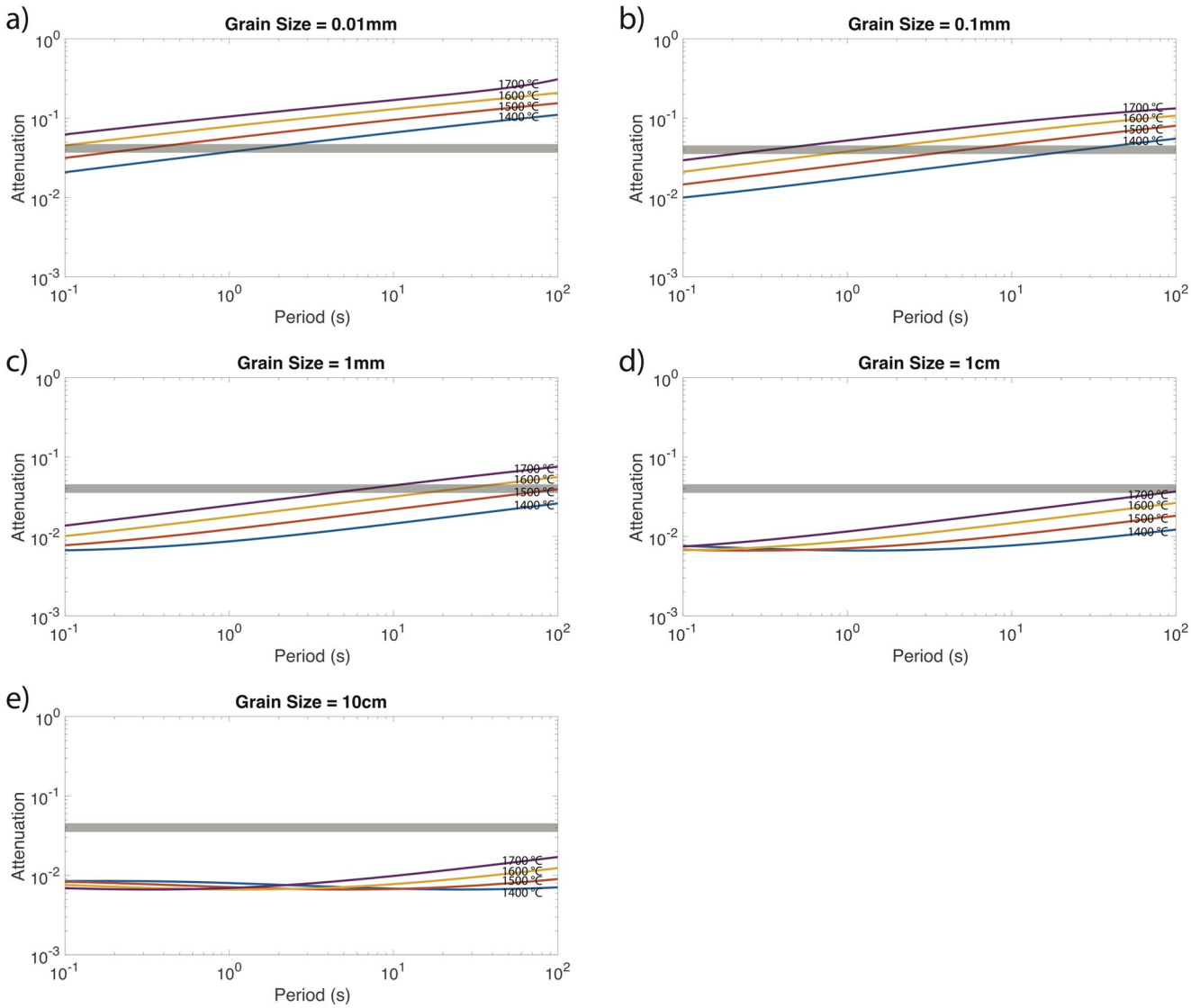

Figure 9. Attenuation values (lines) predicted by the model of Jackson and Faul (2010) using the Very Broadband Rheology Calculator (Havlin et al., 2021; Holtzman, 2016). Attenuation is plotted as a function of seismic wave period (in s) for a range of temperatures for grain sizes of (a) 0.01 mm, (b) 0.1 mm, (c) 1 mm, (d) 1 cm, and (e) 10 cm. We calculate attenuation values for a range of temperatures, indicated by the color of the lines (blue: 1400°C; orange: 1500°C; yellow: 1600°C; and purple: 1700°C). Gray shaded area indicates the range of attenuation values permitted by the observations beneath Mid-Atlantic Geophysical Integrative Collaboration.

the model of Jackson and Faul (2010). Figure 9 shows predicted $Q_S{}^{-1}$ as a function of seismic wave period for a range of temperatures at different grain sizes. Reiterating the arguments from Byrnes et al. (2019), these diagrams demonstrate that only unreasonably small grain sizes and high temperatures can achieve the attenuation measurements (values between 22 and 28 for Q_S) for the region (for a typical seismic wave period of 1–10 s). Attenuation values from Byrnes et al. (2019) can be explained with temperatures around 1400°C, but only with extremely small grain sizes (0.01–0.1 mm). For larger and more realistic grain sizes (1 mm–10 cm), only temperatures of 1700°C and higher are consistent with the attenuation observations (Figures 9c–9e). Since these temperatures and grain-sizes are unlikely for this region (indeed, 1700°C would be above the dry solidus), a purely thermal anomaly cannot explain the CAA attenuation measurements, and additional factors such as the presence of partial melt must be invoked (Byrnes et al., 2019).

4.2.2. Effects of Partial Melt or a Pre-Melting Mechanism

As discussed by Byrnes et al. (2019), the "pre-melting" effect proposed by Yamauchi and Takei (2016) would predict a Q_P value of 102 underneath the Central Appalachians based on conditions relevant for the region

(potential temperature of 1400°C at 150 km, a period of 0.5 s for the incoming wave, an upper mantle viscosity of 10^{18} Pa s, and a Q_P/Q_S ratio of 2.25). This prediction is not consisted with the Q_P values of 50–63 estimated from MAGIC seismic data, which suggests that other mechanisms, such as the presence of partial melt, are needed. However, Byrnes et al. (2019) noted that if the amplitude of the low V_s anomaly is greater than that suggested by tomographic models (specifically that of Schmandt & Lin, 2014), then the pre-melting model of Yamauchi and Takei (2016) could be reconciled with the observations. The pre-melting model can explain velocities as low as approximately 4.1 km/s at 150 km depth (given the trade-offs between the period and viscosity parameters in the Yamauchi and Takei (2016) model) if the temperature is not allowed to exceed 1450° C (Havlin et al., 2021). Assuming a reference velocity of 4.5 km/s, a ∼9% shear velocity reduction (on the low end of our estimated range of 9.1%–13.7%) suggests an absolute V_s of ∼4.1 km/s. Therefore, the pre-melting model could plausibly explain the attenuation observations at the lower end of the maximum velocity reduction or if the ideal reference velocity for the study area is higher than 4.5 km/s.

The presence of partial melt enhances seismic attenuation, as observed in experimental studies for melt-bearing olivine (Chantel et al., 2016; Faul et al., 2004; Jackson et al., 2004). Jackson et al. (2004) observed a prominent broad dissipation peak associated with the presence of partial melt, with the amplitude of the peak increasing with the amount of partial melt in the olivine samples. When extrapolated to upper mantle conditions, the melt-related peak could be a likely explanation for the increased attenuation observed in partially molten regions in the Earth's interior (Faul et al., 2004). The precise amount of melt required varies with temperature and grain size; however, a melt fraction of approximately 1% would be enough to explain the estimated attenuation values for the CAA ($10^{-1.45}$ to $10^{-1.35}$ for ${Q_S}^{-1}$), assuming a temperature of 1250°C and 1 cm grain size (Faul et al., 2004). Experiments conducted at ultrasonic frequencies on melt-bearing olivine (Chantel et al., 2016) can also plausibly explain our results. At seismic frequencies, the experimental results of Chantel et al. (2016) can explain a Q_S value of 25 (corresponding to a Q_P value of ∼56) with a melt fraction as low as 0.5%. The extrapolation to seismic frequencies assumes a power law frequency dependence based on melt-free samples, which may be valid for the relatively low melt fractions inferred (Chantel et al., 2016).

We conclude that the presence of ∼1% partial melt (or less) in the CAA upper mantle is consistent with the experimental predictions for the effect of melt on attenuation and with our observational results. However, the pre-melting effect proposed by Yamauchi and Takei (2016) may also lower the value of Q enough to explain the observations, so we cannot say that partial melt is strictly required to explain the attenuation measurements.

4.2.3. Effects of Water and Composition

Water could potentially influence seismic wave attenuation, but there are conflicting views reported in experimental results (Aizawa et al., 2008; Cline et al., 2018). Experiments studying the effect of water on attenuation are difficult to perform and few have been published. A preliminary study on natural olivine-rich dunite found that attenuation is greatly enhanced in water-rich samples when compared to the corresponding dry samples, but this study did not quantify the effect (Aizawa et al., 2008). However, a recent systematic study on synthetic olivine argued that attenuation is insensitive to water content (Cline et al., 2018). The results from these studies seem to contradict one another; we note, however, that Cline et al. (2018) doped their samples with excess Ti to control water content (H content), and this may account for the discrepancy. Specifically, an excess amount of Ti may plausibly affect the mobility (and diffusion) of the H-related defect, and thus may affect seismic attenuation. It remains possible, therefore, that water enhances attenuation, but since there is as yet no definite evidence on its effect, we cannot firmly conclude whether or not water can be the cause for the attenuation measurements inferred for the CAA. Because seismic attenuation is relatively insensitive to changes in major element chemistry (Karato, 2008), compositional variations are not a plausible explanation for the variations in seismic attenuation documented by Byrnes et al. (2019).

4.3. Electrical Conductivity

Evans et al. (2019) combined MT data with *S*-to-*P* receiver functions to interpret the upper mantle structure beneath the Central Appalachians. A 2-D inversion of the MT data from Evans et al. (2019) is shown in Figure 10. This model suggests variable lithospheric thickness along the MAGIC array, consistent with the results from the receiver function analysis, with a lithospheric thickness of roughly 80 km directly above the CAA. A region of highly conductive asthenospheric upper mantle associated with the CAA is inferred to lie

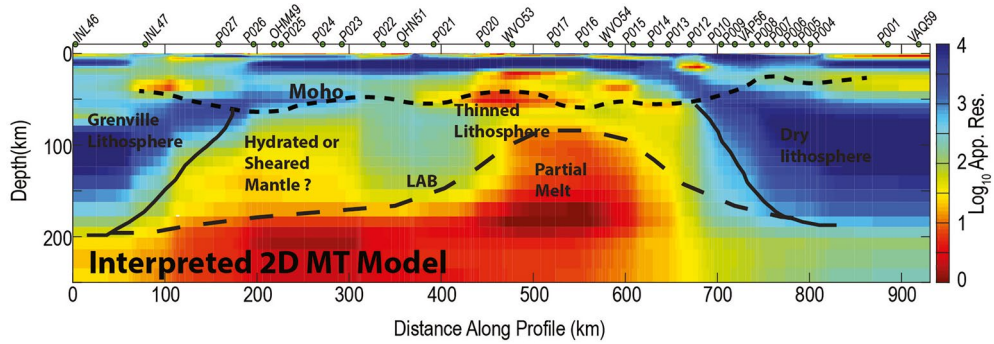

Figure 10. Interpreted 2-D electrical conductivity model across the Mid-Atlantic Geophysical Integrative Collaboration profile, lightly modified from Evans et al. (2019). Background colors show resistivity values, as indicated by the color bar at right. The likely location of the Moho, as inferred from receiver function analysis (Long et al., 2019), is shown with a short dashed line. The edges of the thick lithospheric blocks to the east and west of the Central Appalachian Anomaly (CAA) (prominent low resistivity anomaly in the center of the profile) are shown with solid black lines. The likely location of the lithosphere-asthenosphere boundary (LAB) is shown with a long dashed line. The lowest resistivity values (highest conductivity values) associated with the CAA are observed at depths between 150 and 200 km, but the high-conductivity anomaly extends up to the base of the lithosphere.

directly beneath the mountains; the CAA region is surrounded by thicker and more resistive lithosphere on either side of the mountain range. Estimated values for electrical conductivity in the CAA asthenosphere from the model of Evans et al. (2019) are as high as 0.1 S/m in the 150–200 km depth range. Evans et al. (2019) argued that the high conductivities observed beneath the Central Appalachians cannot be explained by increased temperatures or the presence of water, but require a small amount of partial melt (less than 1%). Here, we expand on the calculations presented in Evans et al. (2019), providing quantitative constraints on the temperatures, partial melt fractions, and water contents needed to explain the conductivity measurements; we also consider the potential effect of composition in explaining the observed CAA conductivity values. In this analysis, we treat the value of 0.1 S/m obtained from the Evans et al. (2019) model as an upper bound on the upper mantle conductivity value.

4.3.1. Effects of Temperature

Dai and Karato (2014) studied the effects of variable iron and water (hydrogen) content on the electrical conductivity of olivine aggregates. They prepared synthetic olivine samples with varying Fe and H contents to measure conductivity at 4 GPa as a function of temperature. To ensure consistent results, they ensured that the difference between the water contents measured for the samples before and after each experiment was not significant (less than 7%) (Dai & Karato, 2014). They found that electrical conductivity was enhanced with increasing iron and water content, as described in Equations 3–5 from Dai and Karato (2014):

$$\sigma = \sigma_{o,\mathrm{wet}} \left(\frac{C_w}{C_{w0}}\right)^r \exp\left(-\frac{H^*_{\mathrm{wet}}}{RT}\right) + \sigma_{o,\mathrm{dry}} \exp\left(-\frac{H^*_{\mathrm{dry}}}{RT}\right) \tag{14}$$

$$\log_{10}\sigma_o = \log_{10}\sigma_{oo} + BX_{\mathrm{Fe}} \tag{15}$$

$$H^* = H^*_o + CX_{\mathrm{Fe}} \tag{16}$$

where $\sigma_{o,\mathrm{wet(dry)}}$ is the wet (dry) pre-exponential factor (dependent on the Fe number, X_{Fe}) and $H^*_{\mathrm{wet(dry)}}$ is the wet (dry) activation enthalpy (also dependent on X_{Fe}). B and C represent the dependence of the pre-exponential factor and activation enthalpy on X_{Fe} respectively. C_w is the water content, C_{w0} the reference water content, and r is an exponent describing the dependence of conductivity on water content. Values for σ_{oo}, H^*_o, B, C, and C_{w0} for wet and dry mechanisms can be found in Table 4 of Dai and Karato (2014). Equations 14–16 allow us to calculate the temperatures needed to explain the conductivity values from Evans et al. (2019). We assume dry conditions and $X_{\mathrm{Fe}} = 0.1$. We find that temperatures greater than 1950°C, unreasonably high (and above the dry solidus), are needed to match the high conductivity values of 0.1 S/m inferred by Evans et al. (2019).

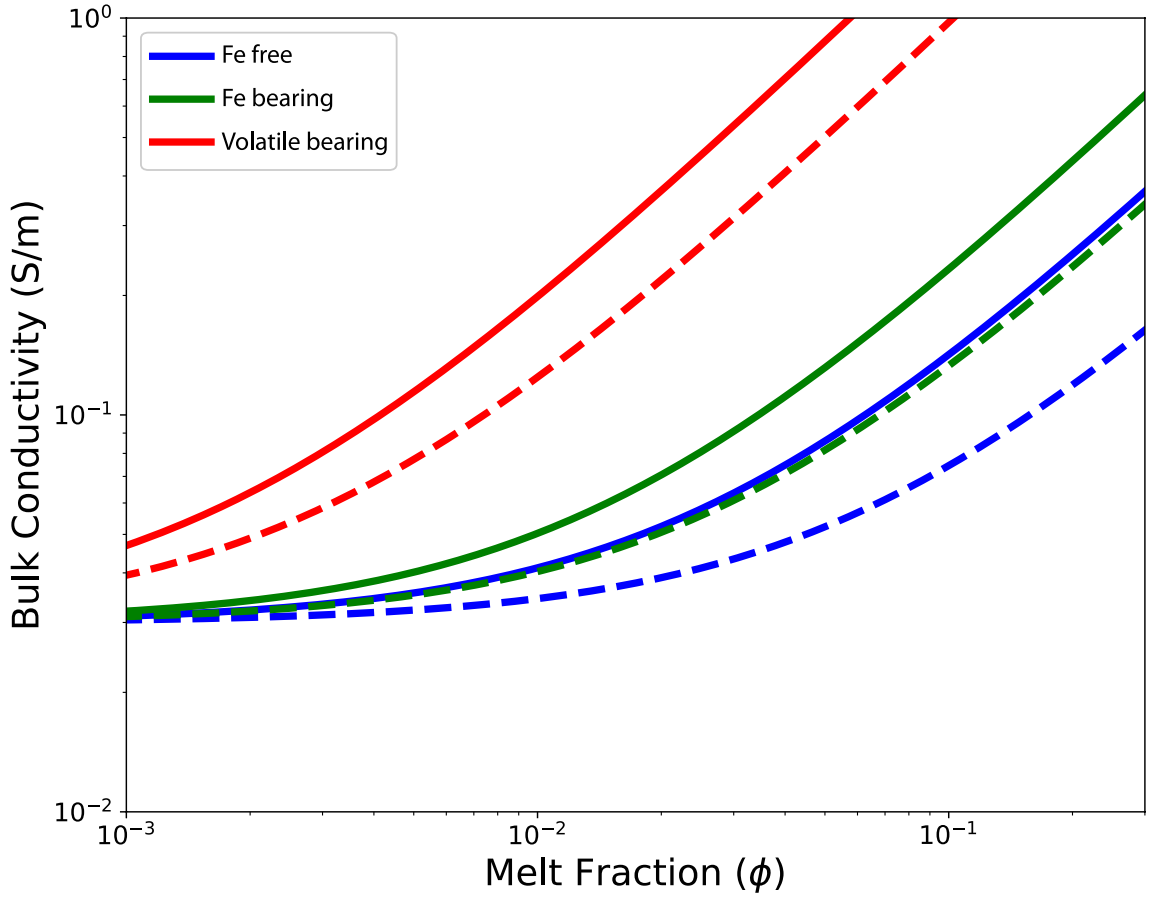

Figure 11. Bulk conductivity as a function of melt fraction for various basaltic melt compositions obtained from SIGMELTS (Pommier & Le-Trong, 2011). Bulk conductivity was calculated assuming a mantle conductivity of 0.03 S/m with different melt compositions indicated by colors (Fe free: Ni et al., 2011; Fe bearing: Tyburczy & Waff, 1983; volatile bearing: Sifré et al., 2014; see legend at top left). Dashed and solid lines indicate conductivities calculated at 1300°C and 1400°C, respectively.

4.3.2. Effects of Partial Melt

Evans et al. (2019) proposed that only a small fraction of partial melt (less than 1%) would be needed to explain the electrical conductivity anomaly associated with the CAA. Here, we expand on their calculations by considering the conductivities of a range of basaltic melts with different compositions and estimating the melt fraction needed to achieve a bulk conductivity of approximately 0.1 S/m. We consider the conductivities of Fe-free basalt (Ni et al., 2011), Fe-bearing basalt (Tyburczy & Waff, 1983), and hydrous, volatile-bearing basalt (Sifré et al., 2014) in these calculations. We use SIGMELTS (Pommier & Le-Trong, 2011), a web application containing a database of electrical conductivity measurements of Earth materials from previous studies, and we calculate the conductivities of the basaltic melts at 1300°C and 1400°C. Fe-free basalts (Ni et al., 2011) have the lowest conductivities (1.43–3.45 S/m). The presence of Fe increases the melt conductivities; for Fe-bearing basalts, conductivities of 3.18–6.18 S/m are inferred (Tyburczy & Waff, 1983). The addition of water and volatiles further dramatically increases the conductivities of melts, as can be seen for basalts with 4.4 wt.% water and 10.4 wt.% CO_2 (28.43–50.69 S/m) (Sifré et al., 2014). Using these melt conductivities, we calculate the conductivity of a mantle with partial melt present by assuming a conductivity value of 0.03 S/m for the solid mantle (following Evans et al., 2019). This calculation relies on a models described by Schmeling (1986) and Hashin and Shtrikman (1962), who developed a set of theoretical models for bulk electrical conductivities of melt-bearing rocks in a variety of geometries. In this calculation, we used the upper Hashin-Shtrikman (HS) bound for the conductivity of a multiphase material. Figure 11 shows the melt fractions required to achieve a conductivity of 0.1 S/m, calculated for a range of partial melt conductivities using a tube geometry model. This demonstrates that depending on the melt composition and temperature, the melt fraction required to match the Evans et al. (2019)

is estimated to be between 0.5% and 15%. This is a large range of possible melt fractions and estimates on the higher end are unrealistic. However, since compositions estimated by Mazza et al. (2014) for the Eocene basalts in the CAA region contain Fe, conductivities calculated for Fe-bearing melts would be most appropriate, and these suggest a required melt fraction closer to ∼1%–2%.

Following the discussion of Evans et al. (2019), we note further that the conductivities of melts could actually even be up to five times higher than those reported in the literature, as melts tend to have a higher Na content during the initiation of melting (Pommier & Garnero, 2014), which increases their conductivities. Therefore, even though consideration of laboratory data of Fe-free basalt (Ni et al., 2011), which has the lowest conductivity due to the absence of Fe and volatiles, suggests that melt fractions of between 3% and 7% would be needed to produce a bulk conductivity of 0.1 S/m (Figure 11), the additional enhancement in conductivity due to Fe and Na could push this melt fraction estimate down substantially. We conclude, therefore, that the asthenospheric conductivity values associated with the CAA can be explained with a model that invokes a modest partial melt fraction (likely 1%–2%), with the most likely scenario being that the melts contain some Na and Fe (Mazza et al., 2014).

Our assumption of ideal melt interconnectivity in our calculation of bulk conductivity, which follows from our use of the upper HS bound (Hashin & Shtrikman, 1962; Schmeling, 1986), is often used for the asthenospheric upper mantle. In any case, our use of the upper HS bound would provide a lower bound on the estimated melt fraction, as any unconnected melt will not impact the conductivity value. Interestingly, our comparison between our seismic observables and the predictions of a partial melt model suggest that melt, if present, may not be in textural equilibrium, and may instead be distributed in dikes or veins (Section 4.1.2). As melt is expected to be in textural equilibrium in the absence of external forcing (e.g., Rudge, 2018), such a melt distribution would require forces such as pressure gradients to be acting on the melt, or for the melt to be undergoing gravity-driven compaction, as discussed in Section 5. Although we have not explicitly calculated effective conductivity for models that include sheets or veins of melt, such a melt configuration would also allow melt to efficiently impact the bulk conductivity of the upper mantle.

4.3.3. Effects of Water and Composition

As discussed by Evans et al. (2019), the magnitude of the effect of water on the conductivity of the upper mantle remains somewhat controversial, despite extensive study (e.g., Dai & Karato, 2014; Karato, 2019; Naif, 2018; Wang et al., 2006; Yoshino & Katsura, 2013; Yoshino et al., 2009). Using the results of Dai and Karato (2014), we can infer the range of water and iron contents that would be consistent with the observed conductivity values. From Equations 14–16 (Dai & Karato, 2014), we infer that only water contents greater than 0.01 wt.% in olivine (with $X_{\mathrm{Fe}} = 0.1$) can achieve the conductivity of 0.1 S/m inferred for the region for a reasonable temperature range (1300°C–1400°C). These values are generally consistent with our understanding of the likely water contents for oceanic asthenosphere (e.g., Hirschmann, 2006; Wang et al., 2006), but are higher than what is thought to be typical of subcontinental mantle (e.g., Wang et al., 2006). As discussed by Evans et al. (2019), therefore, it is likely that water enrichment is not sufficient to explain the observed electrical conductivity values, and other mechanisms such as partial melt are likely involved.

When it comes to compositional variations, even considering a very high iron content (with an Fe number of 1 for the fayalite endmember) for dry olivine, Fe content cannot explain the required conductivity. Assuming upper mantle temperatures between 1300°C and 1400°C, Equations 14–16 (Dai & Karato, 2014) predict conductivity values in the range of 0.02–0.03 S/m for the fayalite endmember, which do not match the observations. Therefore, we conclude that neither increased water content nor increased iron content are satisfactory explanations for the CAA electrical conductivity anomaly.

5. Discussion

The arguments presented in Section 4 about the range of temperatures, water contents, partial melt fractions, and iron contents that can individually explain each of our geophysical observables can be considered together as a whole to suggest a model for the CAA that can explain all the observations. As argued above, a purely thermal anomaly (in which the temperature is below the solidus) can potentially explain both the seismic velocity ratios ($\Delta v_S/\Delta v_P$) and the attenuation observations (if the effect of the pre-melting mechanism of Yamauchi and Takei (2016) is maximized), but it cannot explain the electrical conductivity values. Anomalously wet mantle, with high water content, is not a good explanation for the $\Delta v_S/\Delta v_P$ observations or the electrical conductivity

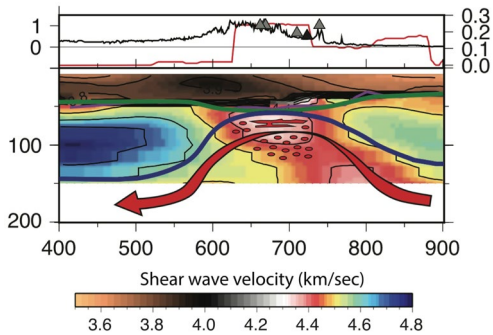

Figure 12. Schematic diagram of the Central Appalachian Anomaly, modified after Long et al. (2021). Top panel shows topography in cross section (black line; scale in km at left), apparent attenuation parameter (Δt_P^*, red line; scale at right) from Byrnes et al. (2019; see also Figure 8), and the location of Eocene (gray triangles) and Late Jurassic (black triangles) volcanic and magmatic products. Bottom panel shows shear wave velocities from the model of Wagner et al. (2018; see colorbar at bottom). Green line indicates location of the Moho; blue line indicates the likely location of the lithosphere-asthenosphere boundary (Evans et al., 2019). Red arrow indicates small-scale mantle flow, likely with a component of upwelling, that maintains the "divot" in the lithosphere and may play a role in generating melt. Partial melt (red shapes) may be ponded in the uppermost asthenosphere but is also likely distributed as deep as ~150–200 km in the upper mantle. (Note that the red shapes are schematic and are not intended to be a literal depiction of melt geometries.)

model; when it comes to attenuation, consensus is still lacking as to whether, and to what extent, water has a meaningful effect (Aizawa et al., 2008; Cline et al., 2018). Local enrichment in Fe cannot reasonably explain the attenuation observations or the electrical conductivity model, and it is unlikely to be a good explanation for the seismic velocity observations. Only the partial melt model can reasonably explain all three observations simultaneously. A small amount of partial melt (~1%–2%) can lower the seismic velocities enough to be consistent with the amplitude of travel time residuals we observe and is consistent with our estimated seismic velocity ratios ($\Delta v_S / \Delta v_P$) as long as the melt is out of textural equilibrium (Takei, 2002). Furthermore, a small partial melt fraction of ~1%–2% can also explain the seismic attenuation and electrical conductivity observations. We conclude that, when taken together, three different lines of geophysical evidence are all consistent with the presence of a small amount of partial melt in the asthenosphere of the CAA, and no alternative explanation can satisfactorily explain the full set of observations. For the case of the CAA, the electrical conductivity constraints have proven to be particularly important to understanding the character of the geophysical anomaly; while enhanced temperature and partial melt can each potentially explain the seismic observables, the conductivity observations are able to definitively rule out a purely thermal anomaly. This helps to illustrate the importance of co-located seismic and MT deployments for constraining the structure and properties of the upper mantle, as also demonstrated by other studies (e.g., Chen et al., 2009; Iwamori et al., 2021; McGary et al., 2014; Moorkamp et al., 2007).

A partially molten asthenospheric upper mantle beneath the Central Appalachians has some important implications for our understanding of formation and evolution of the CAA. Previous studies have suggested that there may have been one or more episodes of lithospheric loss beneath the Central Appalachians in the geologic past, with the most recent episode likely resulting in upwelling return flow, decompression melting, and magmatic and volcanic activity during the Eocene (Mazza et al., 2014). Geophysical imaging of thin lithosphere beneath the Central Appalachians (Byrnes et al., 2019; Evans et al., 2019) have lent support to this interpretation. Recently, Long et al. (2021) evaluated a suite of possible models for the formation and evolution of the CAA and proposed a model that invokes lithospheric loss (likely via a gravity-driven Rayleigh-Tayler instability) during the Eocene, with ongoing small-scale mantle flow that has maintained the thin lithosphere through time. This conceptual model, shown as a sketch in Figure 12, invokes ongoing small-scale mantle flow and upwelling beneath the lithospheric "divot"; this upwelling produces partial melt in the shallowest upper mantle. In this study, we have provided additional support for the idea that the asthenospheric upper mantle in the CAA region contains partial melt today. While our observations do not provide tight constraints on the distribution of partial melt with depth, the fact that the electrical conductivity model of Evans et al. (2019) exhibits relatively high conductivity values to depths of ~150–200 km suggests that some partial melt may be present relatively deep in the upper mantle.

The model shown in Figure 12 invokes the continuous replenishing of the partial melt via ongoing small-scale mantle flow and upwelling. An alternative scenario, however, is that partial melt is not being continuously produced, but rather that the melt (which may have been produced during the Eocene lithospheric loss episode) is dynamically stable in the upper mantle. In order for such a partial melt layer to be geophysically detectable, the compaction length must be sufficiently large. Depending on the relative density of the melt, the melt could be transported upward or downward; thus, the stability of an appropriate amount of melt in the upper mantle would need to be explained (Karato, 2014). Using the model of Richter and McKenzie (1984), the compaction length, δ_C, for melt that is lighter than the surrounding rock and migrates upward can be expressed as

$$\delta_C = \sqrt{\frac{k\eta_S}{\eta_M}}, \tag{17}$$

where k is the permeability of the melt (dependent on the melt fraction and grain size), η_S is the viscosity of the solid skeleton, and η_M is the viscosity of the melt. Using the values for the material properties from Table 1 of

Richter and McKenzie (1984) for a nominal 2% melt fraction ($k = 7.2 \times 10^{-12}$ m^2 assuming a grain size of few cm, $\eta_S = 10^{18}$ Pa s, $\eta_M = 1$ Pa s), the compaction length of the melt would be just a few km. The melt layer accumulated in a region with this compaction length would be too thin to be detected geophysically. However, as we are investigating the possibility of the presence of partial melt in the asthenosphere as deep as 100–200 km depth, the viscosity of the solid skeleton might actually be higher than the value used by Richter and McKenzie (1984). If we assume the viscosity of the solid skeleton to be approximately the same as the viscosity of the upper asthenosphere, 10^{21} Pa s, then melt would be accumulated with a compaction length closer to 85 km, which would imply a thick enough partially molten region for geophysical detection.

In any case, whether the melt is dynamically stable or whether it is being continually replenished via small-scale mantle flow and ongoing upwelling, there is strong evidence from geophysical observations that there is partial melt in the upper mantle (depths shallower than ~200 km) beneath the Central Appalachians today. As discussed by Long et al. (2021), this has some interesting implications for our understanding of the relationships between the production of melt in the upper mantle and its expression (or non-expression) in terms of surface volcanism or magmatic activity, given the lack of contemporaneous volcanism in the Central Appalachians. Long et al. (2021) proposed that the present-day melt fractions in the upper mantle may be too low (perhaps infinitesimal) to produce a volcanic eruption. While Long et al. (2021) speculated that the geophysical anomalies could perhaps be explained by very small melt fractions, the quantitative analysis presented here suggests that melt fractions of ~1%–2% associated with the CAA are likely. As an alternative scenario, Long et al. (2021) proposed that the mantle lithosphere and/or the crust above the CAA may be essentially impermeable, such that partial melt present in the shallow asthenosphere cannot migrate to the surface. If this is the case, then it of course raises the question of why melt was able to reach the surface in this region during the Eocene. Havlin et al. (2013) proposed a model for episodic dike propagation from the accumulation of melt at the lithosphere-asthenosphere boundary, with very rapid timescales for dike injection, which may be relevant for the CAA. We can hypothesize that changes in the tectonic stress field may make it more or less difficult for accumulating melt to migrate through the crust and/or mantle lithosphere, particularly if migrating melt takes advantage of preexisting structures, but this is speculative. In any case, however, this region of the Central Appalachians hosts partial melt in the upper mantle with no-present day volcanic activity, and thus represents an interesting case study for the behavior of partial melt in the sub-continental asthenosphere.

6. Summary

We have presented new observations of P and S wave travel time residuals across the MAGIC array that constrain the likely maximum amplitude of the P and S wave velocity anomalies, as well as the ratio of S to P wave travel time perturbations (and, with some assumptions, the ratio of velocity perturbations $\Delta v_S / \Delta v_P$). We then combined these constraints with previously published observations of seismic attenuation (Byrnes et al., 2019) and electrical conductivity (Evans et al., 2019) beneath MAGIC and systematically investigated the range of upper mantle properties (temperature, partial melt content, water content, and composition) that are consistent with the full suite of observations. We find that an upper mantle anomaly that is purely thermal or that involves variations in water or iron content is not consistent with the geophysical observations. However, the presence of 1%–2% partial melt in the CAA asthenosphere is consistent with multiple types of geophysical observations, with some important implications for our understanding of how the CAA has evolved through time.

Data Availability Statement

Data used in this paper are publicly available via the Incorporated Research Institutions for Seismology (IRIS) Data Management Center (DMC) at https://ds.iris.edu/ds/nodes/dmc. These include seismic waveform data from the MAGIC seismic experiment (network code 7A; https://doi.org/10.7914/XN/7A_2013), the U.S. National Seismic Network (network code US; https://doi.org/10.7914/SN/US), and the EarthScope USArray Transportable Array (network code TA; https://doi.org/10.7914/SN/TA), as well as transfer functions from the MAGIC magnetotelluric experiment (network code EM; https://doi.org/10.17611/DP/EMTF/MAGIC).

Acknowledgments
The MAGIC geophysical experiment (Long et al., 2020) was supported by the EarthScope and GeoPRISMS programs of the National Science Foundation (NSF) via Grant EAR-1251515 to Yale University, Grant EAR-1251329 to the College of New Jersey, and Grant EAR-1460257 to the Woods Hole Oceanographic Institution. The authors thank the many landowners and field volunteers who made the MAGIC seismic and MT deployments possible. Support from the Incorporated Research Institutions for Seismology (IRIS) PASSCAL program was invaluable to the success of the MAGIC seismic experiment. The facilities of the IRIS Consortium are supported by the National Science Foundation's Seismological Facilities for the Advancement of Geoscience (SAGE) Award under Cooperative Support Agreement EAR-1851048. The authors are grateful to scientific collaborators on the MAGIC experiment and related projects for useful discussions. The authors thank Shun Karato for helpful discussions and suggestions. The authors thank Karin Sigloch and an anonymous reviewer for thoughtful and constructive comments that improved the paper.

References

Aizawa, Y., Barnhoorn, A., Faul, U. H., Fitz Gerald, J. D., Jackson, I., & Kovacs, I. (2008). Seismic properties of Anita Bay dunite: An exploratory study of the influence of water. *Journal of Petrology*, *49*(4), 841–855. https://doi.org/10.1093/petrology/egn007

Allen, R. M., Nolet, G., Morgan, W. J., Vogfjörd, K., Bergsson, B. H., Erlendsson, P., et al. (1999). The thin hot plume beneath Iceland. *Geophysical Journal International*, *37*(1), 51–63. https://doi.org/10.1046/j.1365-246x.1999.00753.x

Aragon, J. C., Long, M. D., & Benoit, M. H. (2017). Lateral variations in SKS splitting across the MAGIC array, central Appalachians. *Geochemistry, Geophysics, Geosystems*, *18*(11), 4136–4155. https://doi.org/10.1002/2017GC007169

Artemieva, I. M., Billien, M., Lévêque, J.-J., & Mooney, W. D. (2004). Shear wave velocity, seismic attenuation, and thermal structure of the continental upper mantle. *Geophysical Journal International*, *157*(2), 607–628. https://doi.org/10.1111/j.1365-246X.2004.02195.x

Babikoff, J. C., & Dalton, C. A. (2019). Long-period Rayleigh wave phase velocity tomography using USArray. *Geochemistry, Geophysics, Geosystems*, *20*(4), 1990–2006. https://doi.org/10.1029/2018GC008073

Bezada, M. J. (2017). Insights into the lithospheric architecture of Iberia and Morocco from teleseismic body-wave attenuation. *Earth and Planetary Science Letters*, *478*, 14–26. https://doi.org/10.1016/j.epsl.2017.08.029

Bezada, M. J., Byrnes, J., & Eilon, Z. (2019). On the robustness of attenuation measurements on teleseismic P waves: Insights from microarray analysis of the 2017 North Korean nuclear test. *Geophysical Journal International*, *218*(1), 573–585. https://doi.org/10.1093/gji/ggz169

Biryol, C. B., Wagner, L. S., Fischer, K. M., & Hawman, R. B. (2016). Relationship between observed upper mantle structures and recent tectonic activity across the Southeastern United States. *Journal of Geophysical Research: Solid Earth*, *121*(5), 3393–3414. https://doi.org/10.1022/2015JB012698

Boyce, A., Bastow, I. D., Golos, E. M., Rondenay, S., Burdick, S., & Van der Hilst, R. D. (2019). Variable modification of continental lithosphere during the Proterozoic Grenville orogeny: Evidence from teleseismic P-wave tomography. *Earth and Planetary Science Letters*, *525*, 115763. https://doi.org/10.1016/j.epsl.2019.115763

Byrnes, J. S., Bezada, M., Long, M. D., & Benoit, M. H. (2019). Thin lithosphere beneath the central Appalachian Mountains: Constraints from seismic attenuation beneath the MAGIC array. *Earth and Planetary Science Letters*, *519*, 297–307. https://doi.org/10.1016/j.epsl.2019.04.045

Cammarano, F., Goes, S., Vacher, P., & Giardini, D. (2003). Inferring upper-mantle temperatures from seismic velocities. *Physics of the Earth and Planetary Interiors*, *138*(3–4), 197–222. https://doi.org/10.1016/S0031-9201(03)00156-0

Carrero Mustelier, E., & Menke, W. (2021). Seismic anomalies in the southeastern North American asthenosphere as characterized with body wave travel times from high-quality teleseisms. *Tectonophysics*, *809*, 228853. https://doi.org/10.1016/j.tecto.2021.228853

Chantel, J., Manthilake, G., Andrault, D., Novella, D., Yu, T., & Wang, Y. (2016). Experimental evidence supports mantle partial mantling in the asthenosphere. *Science Advances*, *2*(5), e1600246. https://doi.org/10.1126/sciadv.1600246

Chen, C.-W., Rondenay, S., Evans, R. L., & Snyder, D. B. (2009). Geophysical detection of relict metasomatism from an Archean (~3.5 Ga) subduction zone. *Science*, *326*(5956), 1089–1091. https://doi.org/10.1126/science.1178477

Cline, C. J., II, Faul, U. H., David, E. C., Berry, A. J., & Jackson, I. (2018). Redox-influenced seismic properties of upper-mantle olivine. *Nature*, *555*(7696), 355–358. https://doi.org/10.1038/nature25764

Dai, L., & Karato, S. (2014). Influence of FeO and H on the electrical conductivity of olivine. *Physics of the Earth and Planetary Interiors*, *237*, 73–79. https://doi.org/10.1016/j.pepi.2014.10.006

Deming, W. E. (1943). *Statistical adjustment of data*. John Wiley & Sons.

Evans, R. L., Benoit, M. H., Long, M. D., Elsenbeck, J., Ford, H. A., Zhu, J., & Garcia, X. (2019). Thin lithosphere beneath the central Appalachian Mountains: A combined seismic and magnetotelluric study. *Earth and Planetary Science Letters*, *519*, 308–316. https://doi.org/10.1016/j.epsl.2019.04.046

Faul, U. H., Fitz Gerald, J. D., & Jackson, I. (2004). Shear wave attenuation and dispersion in melt-bearing olivine polycrystals: 2. Microstructural interpretation and seismological implications. *Journal of Geophysical Research*, *109*(B6), B06202. https://doi.org/10.1029/2003JB002407

Golos, E. M., Fang, H., Yao, H., Zhang, H., Burdick, S., Vernon, F., et al. (2018). Shear wave tomography beneath the United States using a joint inversion of surface and body waves. *Journal of Geophysical Research: Solid Earth*, *123*(6), 5169–5189. https://doi.org/10.1029/2017JB014894

Hashin, Z., & Shtrikman, S. (1962). A variational approach to the theory of effective magnetic permeability of multiphase materials. *Journal of Applied Physics*, *33*(10), 3125–3131. https://doi.org/10.1063/1.1728579

Havlin, C., Holtzman, B. K., & Hopper, E. (2021). Inference of thermodynamic state in the asthenosphere from anelastic properties, with applications to the North American upper mantle. *Physics of the Earth and Planetary Interiors*, *314*, 106639. https://doi.org/10.1016/j.pepi.2020.106639

Havlin, C., Parmentier, E. M., & Hirth, G. (2013). Dike propagation driven by melt accumulation at the lithosphere-asthenosphere boundary. *Earth and Planetary Science Letters*, *376*, 20–28. https://doi.org/10.1016/j.epsl.2013.06.010

Hirschmann, M. M. (2006). Water, melting, and the deep Earth H_2O cycle. *Annual Review of Earth and Planetary Sciences*, *34*(1), 629–653. https://doi.org/10.1146/annurev.earth.34.031405.125211

Holtzman, B. K. (2016). Questions on the existence, persistence, and mechanical effects of a very small melt fraction in the asthenosphere. *Geochemistry, Geophysics, Geosystems*, *17*(2), 470–484. https://doi.org/10.1002/2015GC006102

Isaak, D. G. (1992). High-temperature elasticity of iron-bearing olivines. *Journal of Geophysical Research*, *97*(B2), 1871–1885. https://doi.org/10.1029/91JB02675

Iwamori, H., Ueki, K., Hoshide, T., Sakuma, H., Ichiki, M., Watanabe, T., et al. (2021). Simultaneous analysis of seismic velocity and electrical conductivity in the crust and uppermost mantle: A forward model and inversion test based on grid search. *Journal of Geophysical Research: Solid Earth*, *126*(9), e2021JB022307. https://doi.org/10.1029/2021JB022307

Jackson, I., & Faul, U. H. (2010). Grainsize-sensitive viscoelastic relaxation in olivine: Towards a robust laboratory-based model for seismological application. *Physics of the Earth and Planetary Interiors*, *183*(1–2), 151–163. https://doi.org/10.1016/j.pepi.2010.09.005

Jackson, I., Faul, U. H., Fitz Gerald, J. D., & Tan, B. H. (2004). Shear wave attenuation and dispersion in melt-bearing olivine polycrystals: 1. Specimen fabrication and mechanical testing. *Journal of Geophysical Research*, *109*(B6), B06201. https://doi.org/10.1029/2003JB002406

Jacobsen, S. D., Jiang, F., Mao, Z., Duffy, T. S., Smyth, J. R., Holl, C. M., & Frost, D. J. (2008). Effects of hydration on the elastic properties of olivine. *Geophysical Research Letters*, *35*(14), L14303. https://doi.org/10.1029/2008GL034398

Karato, S. (1993). Importance of anelasticity in the interpretation of seismic tomography. *Geophysical Research Letters*, *20*(15), 1623–1626. https://doi.org/10.1029/93GL01767

Karato, S. (2008). *Deformation of Earth materials: An introduction to the rheology of solid Earth*. Cambridge University Press. https://doi.org/10.1017/CBO9780511804892

Karato, S. (2014). Does partial melting explain geophysical anomalies? *Physics of the Earth and Planetary Interiors*, *228*, 300–306. https://doi.org/10.1016/j.pepi.2013.08.006

Karato, S. (2019). Some remarks on hydrogen-assisted electrical conductivity in olivine and other minerals. *Progress in Earth and Planetary Science*, *6*(1), 55. https://doi.org/10.1186/s40645-019-0301-2

Karato, S., Jung, H., Katayama, I., & Skemer, P. (2008). Geodynamic significance of seismic anisotropy of the upper mantle: New insights from laboratory studies. *Annual Review of Earth and Planetary Sciences*, *36*(1), 59–95. https://doi.org/10.1146/annurev.earth.36.031207.124120

Karato, S., & Spetzler, H. A. (1990). Defect microdynamics in minerals and solid-state mechanisms of seismic wave attenuation and velocity dispersion in the mantle. *Reviews of Geophysics*, *28*(4), 399–421. https://doi.org/10.1029/RG028i004p00399

Kennett, B. L. N., Engdahl, E. R., & Buland, R. (1995). Constraints on seismic velocities in the Earth from traveltimes. *Geophysical Journal International*, *122*(1), 108–124. https://doi.org/10.1111/j.1365-246X.1995.tb03540.x

Krauss, Z., & Menke, W. (2020). The Northern Gulf Anomaly: P- and S-wave travel time delays illuminate a strong thermal feature beneath the Northern Gulf of Mexico. *Earth and Planetary Science Letters*, *534*, 116102. https://doi.org/10.1016/j.epsl.2020.116102

Lee, H. (2021). *An exploration of the effect of anisotropy on seismic tomography in different geological settings* (PhD thesis). University of Minnesota. Retrieved from https://hdl.handle.net/11299/224668

Levin, V., Lerner-Lam, A., & Menke, W. (1995). Anomalous mantle structure at the Proterozoic-Paleozoic boundary in northeastern U.S. *Geophysical Research Letters*, *22*(2), 121–124. https://doi.org/10.1029/94GL02693

Levin, V., Long, M. D., Skryzalin, P., Li, Y., & López, I. (2018). Seismic evidence for a recently formed mantle upwelling beneath New England. *Geology*, *46*(1), 87–90. https://doi.org/10.1130/G39641.1

Levin, V., Menke, W., & Lerner-Lam, A. (1996). Seismic anisotropy in the north-eastern US as a source of significant teleseismic P traveltime anomalies. *Geophysical Journal International*, *126*(2), 593–603. https://doi.org/10.1111/j.1365-246X.1996.tb05312.x

Long, M. D., Benoit, M. H., Aragon, J. C., & King, S. D. (2019). Seismic imaging of mid-crustal structure beneath central and eastern North America: Possibly the elusive Grenville deformation? *Geology*, *47*(4), 371–374. https://doi.org/10.1130/G46077.1

Long, M. D., Benoit, M. H., Evans, R. L., Aragon, J. C., & Elsenbeck, J. (2020). The MAGIC Experiment: A combined seismic and magnetotelluric deployment to investigate the structure, dynamics, and evolution of the central Appalachians. *Seismological Research Letters*, *91*(5), 2960–2975. https://doi.org/10.1785/0220200150

Long, M. D., Jackson, K. G., & McNamara, J. F. (2016). *SKS* splitting beneath Transportable Array stations in eastern North America and the signature of past lithospheric deformation. *Geochemistry, Geophysics, Geosystems*, *17*(1), 2–15. https://doi.org/10.1002/2015GC006088

Long, M. D., Wagner, L. S., King, S. D., Evans, R. L., Mazza, S. E., Byrnes, J. S., et al. (2021). Evaluating models for lithospheric loss and intraplate volcanism beneath the Central Appalachian Mountains. *Journal of Geophysical Research: Solid Earth*, *126*(10), e2021JB022571. https://doi.org/10.1019/2021JB022571

Mazza, S. E., Gazel, E., Johnson, E. A., Bizimis, M., McAleer, R., & Biryol, C. B. (2017). Post-rift magmatic evolution of the eastern North American "passive-aggressive" margin. *Geochemistry, Geophysics, Geosystems*, *18*(1), 3–22. https://doi.org/10.1002/2016GC006646

Mazza, S. E., Gazel, E., Johnson, E. A., Kunk, M. J., McAleer, R., Spotila, J. A., et al. (2014). Volcanoes of the passive margin: The youngest magmatic event in eastern North America. *Geology*, *42*(6), 483–486. https://doi.org/10.1130/G35407.1

McGary, R. S., Evans, R. L., Wannamaker, P. E., Elsenbeck, J., & Rondenay, S. (2014). Pathway from subducting slab to surface for melt and fluids beneath Mount Rainier. *Nature*, *511*(7509), 388–340. https://doi.org/10.1038/nature13493

Menke, W., Lamoureux, J., Abbott, D., Hopper, E., Hutson, D., & Marrero, A. (2018). Crustal heating and lithospheric alteration and erosion associated with asthenospheric upwelling beneath southern New England (USA). *Journal of Geophysical Research: Solid Earth*, *123*(10), 8995–9008. https://doi.org/10.1029/2018JB015921

Menke, W., Skryzalin, P., Levin, V., Harper, T., Darbyshire, F., & Dong, T. (2016). The Northern Appalachian Anomaly: A modern asthenospheric upwelling. *Geophysical Research Letters*, *43*(19), 10173–10179. https://doi.org/10.1002/2016GL070918

Moorkamp, M., Jones, A. G., & Eaton, D. W. (2007). Joint inversion of teleseismic receiver functions and magnetotelluric data using a genetic algorithm: Are seismic velocities and electrical conductivities compatible? *Geophysical Research Letters*, *34*(16), L16311. https://doi.org/10.1029/2007GL030519

Naif, S. (2018). An upper-bound on the conductivity of hydrated oceanic mantle at the onset of dehydration melting. *Earth and Planetary Science Letters*, *482*, 357–388. https://doi.org/10.1016/j.epsl.2017.11.024

Nestola, F., Pasqual, D., Smyth, J. R., Novella, D., Secco, L., Manghnani, M. H., & Dal Negro, A. (2011). New accurate elastic parameters for the forsterite-fayalite solid solution. *American Mineralogist*, *96*(11–12), 1742–1747. https://doi.org/10.2138/am.2011.3829

Ni, H., Keppler, H., & Behrens, H. (2011). Electrical conductivity of hydrous basaltic melts: Implications for partial melting in the upper mantle. *Contributions to Mineralogy and Petrology*, *162*(3), 637–650. https://doi.org/10.1007/s00410-011-0617-4

Pommier, A., & Garnero, E. J. (2014). Petrology-based modeling of mantle melt electrical conductivity and joint interpretation of electromagnetic and seismic results. *Journal of Geophysical Research: Solid Earth*, *119*(5), 4001–4016. https://doi.org/10.1002/2013JB010449

Pommier, A., & Le-Trong, E. (2011). "SIGMELTS": A web portal for electrical conductivity calculations in geosciences. *Computers & Geosciences*, *37*(9), 1450–1459. https://doi.org/10.1016/j.cageo.2011.01.002

Porter, R., Liu, Y., & Holt, W. E. (2015). Lithospheric records of orogeny within the continental U.S. *Geophysical Research Letters*, *43*(1), 144–153. https://doi.org/10.1002/2015GL066950

Richards, P. G., & Menke, W. (1983). The apparent attenuation of a scattering medium. *Bulletin of the Seismological Society of America*, *73*, 1005–1021. https://doi.org/10.1785/BSSA0730041005

Richter, F. M., & McKenzie, D. (1984). Dynamical models for melt segregation from a deformable matrix. *The Journal of Geology*, *92*(6), 729–740. https://doi.org/10.1086/628908

Romanowicz, B., & Durek, J. J. (2000). Seismological constraints on attenuation in the Earth: A review. In S.-I. Karato, A. Forte, R. Liebermann, G. Masters, & L. Stixrude (Eds.), *Earth's deep interior: Mineral physics and tomography from the atomic to the global scale*, *Geophysical Monograph Series* (Vol. 117, pp. 161–179). American Geophysical Union.

Rudge, J. F. (2018). Textural equilibrium melt geometries around tetrakaidecahedral grains. *Proceedings of the Royal Society A*, *474*(2212), 20170639. https://doi.org/10.1098/rspa.2017.0639

Savage, B., Covellone, B. M., & Shen, Y. (2017). Wave speed structure of the eastern North American margin. *Earth and Planetary Science Letters*, *459*, 394–405. https://doi.org/10.1016/j.epsl.2016.11.028

Schmandt, B., & Lin, F.-C. (2014). P and S wave tomography of the mantle beneath the United States. *Geophysical Research Letters*, *41*(18), 6342–6349. https://doi.org/10.1002/2014GL061231

Schmeling, H. (1986). Numerical models on the influence of partial melt on elastic, anelastic and electrical properties of rocks. Part II: Electrical conductivity. *Physics of the Earth and Planetary Interiors*, *43*(2), 123–126. https://doi.org/10.1016/0031-9201(86)90080-4

Shen, W., & Ritzwoller, M. H. (2016). Crustal and uppermost mantle structure beneath the United States. *Journal of Geophysical Research: Solid Earth*, *121*(6), 4306–4342. https://doi.org/10.1002/2016JB012887

Sifré, D., Gardés, E., Massuyeau, M., Hashim, L., Hier-Majumder, S., & Gaillard, F. (2014). Electrical conductivity during incipient melting in the oceanic low-velocity zone. *Nature*, *509*(7498), 81–85. https://doi.org/10.1038/nature13245

Sigloch, K., & Nolet, G. (2006). Measuring finite-frequency body-wave amplitudes and traveltimes. *Geophysical Journal International*, *167*(1), 271–287. https://doi.org/10.1111/j.1365-246X.2006.03116.x

Speziale, S., Jiang, F., & Duffy, T. S. (2005). Compositional dependence of the elastic wave velocities of mantle minerals: Implications for seismic properties of mantle rocks. In R. D. van der Hilst, J. D. Bass, J. Matas, & J. Trampert (Eds.), *Earth's deep mantle: Structure, composition, and evolution* (Vol. 160, pp. 301–320). American Geophysical Union. https://doi.org/10.1029/160GM18

Takei, Y. (2002). Effect of pore geometry on V_P/V_S: From equilibrium geometry to crack. *Journal of Geophysical Research*, *107*(B2), 2043. https://doi.org/10.1029/2001JB000522

Tyburczy, J. A., & Waff, H. S. (1983). Electrical conductivity of molten basalt and andesite to 25 kilobars pressure: Geophysical significance and implications for charge transport and melt structure. *Journal of Geophysical Research*, *88*(B3), 2413–2430. https://doi.org/10.1029/JB088iB03p02413

Wagner, L. S., Fischer, K. M., Hawman, R., Hopper, E., & Howell, D. (2018). The relative roles of inheritance and long-term passive margin lithospheric evolution on the modern structure and tectonic activity in the southeastern United States. *Geosphere*, *14*(4), 1385–1410. https://doi.org/10.1130/GES01593.1

Wang, D., Mookherjee, M., Xu, Y., & Karato, S. (2006). The effect of water on the electrical conductivity in olivine. *Nature*, *443*(7114), 977–908. https://doi.org/10.1038/nature05256

Yamauchi, H., & Takei, Y. (2016). Polycrystal anelasticity at near-solidus temperatures. *Journal of Geophysical Research: Solid Earth*, *121*(11), 7790–7820. https://doi.org/10.1002/2016JB013316

Yoshino, T., & Katsura, T. (2013). Electrical conductivity of mantle minerals: Role of water in conductivity anomalies. *Annual Review of Earth and Planetary Sciences*, *41*(1), 605–628. https://doi.org/10.1146/annurev-earth-050212-124022

Yoshino, T., Matsuzaki, T., Shatskiy, A., & Katsura, T. (2009). The effect of water on the electrical conductivity of olivine aggregates and its implications for the electrical structure of the upper mantle. *Earth and Planetary Science Letters*, *288*(1–2), 291–300. https://doi.org/10.1016/j.epsl.2009.032